https://doi.org/10.5194/egusphere-2025-2840
Preprint. Discussion started: 10 July 2025

Formation of mineral-associated organic matter via rock weathering: an experimental test for the organo-metallic glue hypothesis

Kaori Matsuoka[1], Jo Jinno[1], Hiroaki Shimada[2], Emi Matsumura[1], Ryo Shingubara[3], Rota Wagai[1]

[1]Institute for Agro-Environmental Sciences, National Agriculture and Food Research Organization, Tsukuba, 305-8604, Japan

[2]Division of Plant Production Science, Section of Plant Production Science Research Center for Global Agromedicine, Obihiro University of Agriculture and Veterinary Medicine, Obihiro, 080-8555, Japan

[3]Research Center for Advanced Analysis, National Agriculture and Food Research Organization, Tsukuba, 305-8604, Japan

Correspondence: Kaori Matsuoka (matsuoka.kaori811@naro.go.jp; kaori.matsuoka@hotmail.co.jp); Rota Wagai (wagai.rota200@naro.go.jp)

Abstract. Mineral-associated organic matter (MAOM), representing the dominant form of relatively stable C in soil, contains high physicochemical heterogeneity. The co-localization of organic matter (OM) with reactive aluminum (Al) and iron (Fe) phases in various MAOM fractions—across a range of natural and cultivated soils from five soil orders—has led to the "organo-metallic glue" hypothesis. The hypothesis proposes that coprecipitates formed between mineral-derived metals and microbially processed OM act as a binding agent, promoting the formation of stable microaggregates and thereby enhancing soil OM persistence. However, the formation mechanism remains unclear as the observed associations reflect multiple soil processes. We thus designed a simple laboratory experiment to test if the supply of metals and metalloids through rock weathering controls MAOM formation and if the OM-to-metal ratio of the material formed is consistent with complexation, sorptive association, or their mixture (i.e., coprecipitates). Two end-member igneous rocks (granite and basalt) crushed to have 38–75 µm size and, additionally, 20–38 µm size for basalt, as well as river sand (100–300 µm) as control were mixed with leaf compost (powdered to 100–250 µm) as single OM source. The mineral-OM mixtures were incubated aerobically at 30 ºC with the natural soil microbial community and subjected to 8 wet-and-dry cycles using artificial rainwater (pH 4.73) over a 55-day experiment. The mixtures were then fractionated by density to examine the formation of meso-density, organo-mineral aggregates (1.8–2.4 g cm^{-3}: MF) by distinguishing it from the compost-dominant low-density fraction (< 1.8 g cm^{-3}: LF) and high-density fraction (>2.4 g cm^{-3}: HF) consisting of the crushed rock. The MF formation assessed as C content was 1.49 ± 0.06 mg C g^{-1} rock (fine basalt), 1.04 ± 0.08 (coarse basalt), and 0.62 ± 0.06 (granite) over the 55 days, while the net MF mass increase was detected only in fine basalt due to the presence of meso-density materials in the crushed rock (< 7% by mass). Faster chemical weathering of the fine basalt was indicated by a significant increase in extractable Fe and Al phases, largely in MF, and the highest leaching of Fe and base cations (esp. Na and Ca). The organo-mineral aggregates formed in the fine basalt treatment had the C-to-metal (Fe+Al) ratio of 0.36 ± 0.01 (molar basis), consistent with organo-metal coprecipitation. Further analysis focusing on the two basalt treatments revealed a significant decline in C:N ratios by 23–25 units and enrichment of $\delta^{13}C$ and $\delta^{15}N$ by 0.9–1.2‰ and 0.6‰, respectively, in MFs compared to LFs, indicating a strong contribution of microbial N-containing compounds to the MAOM formation. While microbial community composition differed among the treatments, no significant difference was found in qPCR-based bacterial number or species richness. Microscopic analyses using SEM and STXM confirmed the presence of shaking-resistant microaggregates and co-localization of C, Fe, and Al in MF from selected MF samples. Together, our results strongly supported the organo-metallic glue hypothesis and provided laboratory evidence of basalt-induced MAOM formation as well as some insights into early pedogenesis and organo-mineral interactions when applying crushed rock to soils.

https://doi.org/10.5194/egusphere-2025-2840
Preprint. Discussion started: 10 July 2025

1 Introduction

Organic matter (OM) in soil plays a fundamental role in global carbon cycling, soil fertility, and ecosystem functioning (Lehmann et al., 2020; Friedlingstein et al., 2022; Angst et al., 2023). Its long-term persistence strongly depends on its physicochemical associations with reactive soil minerals such as aluminosilicate clays and metal oxides that have a high specific surface area (e.g., Sørensen, 1972; Baldock and Skjemstad, 2000; Wattel-Koekkoek et al., 2003; Saidy et al., 2015; Hemingway et al., 2019). One group of reactive minerals is pedogenic metal and metalloid phases (mainly iron (Fe), aluminum (Al), and silicon (Si)), weathering products of Fe-, Al-, and/or Si-bearing minerals during soil development. They can be present as mono or polymeric species complexed with organic ligands or as oxides such as short-range-ordered (SRO) aluminosilicates and metal oxides, as well as high-crystallinity Fe and Al oxides (e.g., Harter and Naidu, 1995; Cornell and Schwertmann, 2003; Parker, 2005; Ashida et al., 2021; Watanabe et al., 2023).

At macro scales, while OM molecular composition exerts some controls depending on ecosystem type and climate (Sollins et al., 1996; Hall et al., 2020), soils rich in pedogenic metals store more OM in soil. For instance, basaltic and andesitic soils have been shown to accumulate higher OM stocks than granitic soils (Orgill et al., 2017; Angst et al., 2018; Dutta et al., 2000; Rasmussen et al., 2005; Mao et al., 2020). Furthermore, pedogenic metal contents positively correlate with soil OM stock and, to some extent, with its C persistence based on radiocarbon analysis (e.g., Torn et al., 1997; Percival et al., 2000; Masiello et al., 2004; Lawrence et al., 2015; Shimada et al., 2022; von Fromm et al., 2025). At the molecular scale (submicron to nano sizes), pedogenic metal phases engage in various interactions with OM, such as cation bridging, adsorption, and coprecipitation, thereby enhancing OM resistance to microbial degradation and dissolution (Kleber et al., 2015). Among these, coprecipitation remains the least understood. Although the chemical composition and formation environments of coprecipitates may vary widely, conceptual advances have been made by comparing soil-derived coprecipitates with synthetic analogs produced under soil-relevant conditions, using electron microscopy and spectroscopy techniques (Basile-Doelsch et al., 2015; Tamrat et al., 2018, 2019; Jamoteau et al., 2023). A remaining key question is the role of these nanoscale coprecipitates on the emergence of larger-scale soil properties such as the development of aggregates and soil pore networks (Asano and Wagai, 2014; Regelink et al., 2015; Rabot et al., 2018; Totsche et al., 2018; Schlüter et al., 2020; Yudina and Kuzyakov, 2023), which strongly regulate microbial and plant root activities and are thus closely tied to soil and ecosystem functioning (Hartmann and Six, 2023; Philippot et al., 2024).

The organo-metallic glue hypothesis (Wagai et al., 2020) may offer a mechanistic bridge between the macro-scale patterns (e.g., C-metal correlations) and the molecular-scale interactions between OM and minerals. The hypothesis, proposed based on the observed co-occurrence of extractable Fe and Al phases with N-enriched OM in meso-density fraction (MF: 1.8–2.4 g cm^{-3}) with relatively constant OC: metal ratios found across 23 soils from 5 soil orders, suggests that Fe and Al dissolved from soil minerals bind with decomposing OM to form organo-metallic glue which binds mineral and organic particles (e.g., clays and fragmented POMs) to form physically-stable microaggregates. However, testing this hypothesis using natural soils is challenging because soils contain diverse OM compounds and multiple metal species as a result of short- and long-term processes. An artificial soil system, which consists of defined mineral and OM components, would be suitable to assess specific OM-mineral interactions, as it has demonstrated the formation of organo-mineral assemblages within short timescales under controlled conditions (Vogel et al., 2014; Pronk et al., 2017; Bucka et al., 2019, 2021), although the effect of mineralogical parameters is largely unexplored.

The current study aimed to examine some aspects of the organo-metallic glue hypothesis using an artificial soil system. We hypothesized that the difference in rock weathering rate (i.e., the supply rate of Fe and Al) controls the formation of organo-mineral assemblage and tested it using two end-member igneous rocks (basalt and granite) crushed to have 38–75 µm size and, additionally, 20–38 µm size for basalt, as well as river sand (100–300 µm) as a control. These minerals were mixed with leaf compost (powdered to 100–250 µm) as a single OM source. Upon inoculation with the soil microbial community, the mineral-OM mixtures were subject to weekly leaching events with artificial rainwater, followed by drying

https://doi.org/10.5194/egusphere-2025-2840
Preprint. Discussion started: 10 July 2025

over a 55-day incubation duration. We quantified the formation of organo-mineral aggregate by density fractionation followed by chemical and, to a limited extent, microscopic characterization of isolated fractions by SEM and STXM-NEXAFS. We showed significant increases in both extractable metals (esp. Fe) and OM in the meso-density fraction from fine basalt-OM mixture and discussed the linkage among microbial heterotrophic activity, chemical weathering, and organo-mineral aggregation.

2 Materials and Methods

We prepared four types of mineral-organic matter (OM) mixtures using crushed rock and river sand with leaf compost, followed by 55-day aerobic incubation with 8 wet-and-dry cycles (Fig. 1). The mixtures after the incubation were destructively sampled and fractionated by density to quantify the organo-mineral assemblage formed.

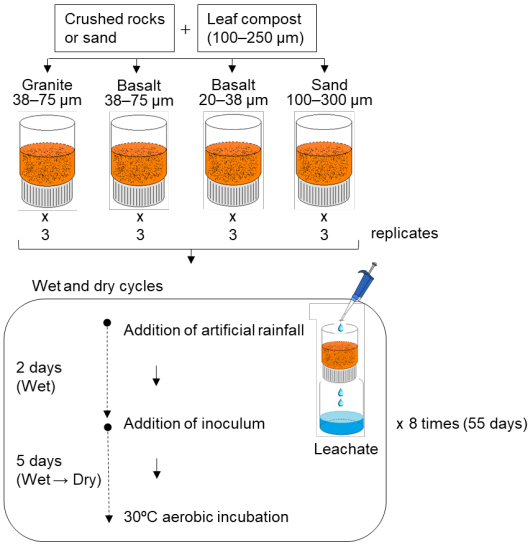

Figure 1. Schematics of the 55-day incubation experiment, including eight wet-and-dry cycles.

2.1 Source materials and preparation for mineral-organic matter mixtures

We selected two rocks having a contrasting chemical composition and weatherability, and a river sand as a control for this study. Basalt, a mafic igneous rock, is characterized by a higher weathering rate and faster formation of SRO Fe and Al minerals compared to felsic rocks such as granite (Gray and Murphy, 2002; Chapman et al., 2009). Crushed granite ("pan" type, ≤ 75 µm, Yoko Bussan Co. Ltd., Hiroshima, Japan) was further ground by a blender (WB-1, Osaka Chemical Co. Ltd., Osaka, Japan), followed by wet sieving to isolate the 38–75 µm particle size class. For crushed basalt ("dust" type, < 2500 µm, Horie-Kenzai Co. Ltd., Akita, Japan), we prepared two particle size classes. Coarse basalt (38–75 µm) was isolated by wet sieving as described above. Fine basalt (20–38 µm) was isolated by repeated sedimentation of < 38 µm materials in deionized water until the supernatant was free of visible particles < 20 µm based on Stokes law. As a mineral component having the least weatherability, river sand (93% SiO_2) with a mean particle size of approximately 100–300 µm (Toyoura Keiseki Kogyo Co., Ltd., Yamaguchi, Japan) was also used in this study. All four rocks obtained were oven-dried at 50 ºC before mixing with OM.

The total elemental compositions of the isolated granite and basalt rocks, determined by XRF analysis (NEX CG, Rigaku

https://doi.org/10.5194/egusphere-2025-2840
Preprint. Discussion started: 10 July 2025

Corporation, Tokyo, Japan; Table S1), were within a common range for respective rock types. Further characterization of the source basalt is reported elsewhere (Yang et al., under review). The total C concentration of the isolated rocks was < 0.3 mg g^{-1} (vario MAX cube, Elementar, Germany). Particle size distribution of the four rock types, assessed by a laser scattering particle distribution analyzer (LA-920, Horiba Ltd., Kyoto, Japan), confirmed the target size ranges (Fig. S1). Briefly, the granite (target size: 38–75 µm) had the mean weight diameter (MWD) of 63.9 µm and the cumulative percentile values (the grain size at which 50% of the grains are coarser, D_{50}) of 55.6 µm (Fig. S1). The coarse basalt (38–75 µm) had a MWD of 59.8 µm and D_{50} of 52.5 µm. The fine basalt (20–38 µm) had a MWD of 28.8 µm and D_{50} of 22.9 µm. The sand (100–300 µm) had a MWD of 267.3 µm and D_{50} of 231.6 µm. The specific surface area of the four mineral components was measured by N_2 gas sorption Autosorb iQ (Quantachrome Corp., Boynton Beach, FL, USA) using a multi-point BET approach (partial pressures of < 0.3) after outgassing under a vacuum at 150 °C.

Leaf compost was used as the single OM source for the mineral-OM mixtures. The compost, produced mainly from tree leaves composted for one year, was the same material annually applied to the long-term, no-till plus leaf compost management in the experimental field of the Institute for Agro-Environmental Sciences, Tsukuba, Japan (Wagai et al., 2013a). The leaf compost was air-dried, ground, and dry-sieved to a size of 100–250 µm. The compost had a C content of 408 mg g^{-1} with a C:N ratio of 41. pH of the compost was 5.92 (H_2O) and 5.45 (KCl). The C structure of the compost had carbonyl-C 7.7%, aromatic-C 9.6%, O-alkyl-C 63.3%, and alkyl-C 19.4% (Fig. S2), which was assessed by solid-state ^{13}C nuclear magnetic resonance (NMR) spectrometry using an FT NMR system (JNM-ECA600II, JEOL Ltd., Tokyo, Japan) according to the procedure by Hiradate et al. (2004). The NMR spectrum was divided into chemical shift regions representative of the four major types of C present: 0–45 ppm (alkyl C), 45–110 ppm (O-alkyl C), 110–165 ppm (aromatic C), 165–210 ppm (carbonyl C) (Golchin et al., 1994). The total signal intensity and the proportion contributed by each C type were determined by the integration of the spectral regions.

The fine and coarse basalt, granite, and river sand (20.0 g each) were well-mixed with 2.50 g of the leaf compost under dry conditions in three replicates. The mineral-OM mixtures prepared had an initial C content of 4.5%, which is the higher end of the C level for cultivated topsoils. The mixtures were then transferred into a 50 mL plastic column with the bottom covered with double layers of nylon mesh sheet (approximately 6 µm mesh size) (Fig. 1).

2.2 Aerobic incubation and repeated leaching with wet/dry cycles

The mineral-OM mixtures were subjected to weekly repeated leaching events using artificial rainwater over a 55-day experimental duration. The artificial rainwater was prepared to represent a common chemical composition of rainwater in Japan based on the data from the acid deposition survey in 2014 (Horie et al., 2016). The chemical composition of rainwater was pH 4.73; SO_4^{2-} 18.1 µmol L^{-1}; NO_3^- 15.4 µmol L^{-1}; Cl^- 90.2 µmol L^{-1}; NH_4^+ 17.9 µmol L^{-1}; Na^+ 76.6 µmol L^{-1}; K^+ 2.62 µmol L^{-1}; Ca^{2+} 5.37 µmol L^{-1}; and Mg^{2+} 9.04 µmol L^{-1}: we used reagents of HCl, KCl, $CaCl_2$, $MgSO_47H_2O$, $NaNO_3$, $(NH_4)_2SO_4$, and NaCl.

The microbial inoculum was prepared from the well-characterized surface soil (0–5 cm) from the long-term experimental field (no-till with leaf compost plot; see above). The soil is classified as Hydric Hapludand (Soil Survey Staff, 2014) and a Hydric-Silic Andosol (IUSS Working Group WRB, 2015). The microbial inoculum was obtained by mixing the field-moist soil with deionized water at a ratio of 1:15, and the mixture was shaken for 30 min with glass beads. After that, the mixture was filtered through a 5-µm membrane filter (slightly modified from Wagai and Sollins, 2002) to keep bacteria and fungal spores/fragments in suspension while removing major grazers. The inoculum was stored in a refrigerator for no more than 24 h before inoculation events.

The incubation was initiated by gently applying 40 mL of artificial rainwater to each column from the surface. The column was left at room temperature overnight, and the leachate was collected. The volume of rainwater added every 7 days was roughly equal to the average annual precipitation of Japan, assuming an even distribution of rainfall events over a year

https://doi.org/10.5194/egusphere-2025-2840
Preprint. Discussion started: 10 July 2025

(Horie et al., 2016). After collecting the leachate, 1 mL of microbial inoculum was added to each column. The water content of the mineral-OM mixtures at this point was 52–63% on an air-dried basis (Table S3). All columns were incubated in the dark at 30 °C for 5 days, which made the water content nearly zero. The clod formed in the column was then physically mixed into small pieces using a spatula. The second wet-and-dry cycle was initiated by applying 40 mL of rainwater again, followed by 0.1 mL of inoculum (instead of 1 mL of inoculum added the first time). The cycle was repeated 8 times over the 55-day incubation duration (Fig. 1). The mineral-OM mixtures after the incubation were gently homogenized and sieved through a 2 mm mesh for further analysis. The leachate collected after each wet-and-dry cycle from each column was combined to analyze the concentrations of dissolved organic C (DOC), Al, Fe, Si, and base cations (Na, Ca, K, and Mg), as well as pH.

2.3 Density fractionation after the incubation

The mineral-OM mixtures were fractionated by density to distinguish organo-mineral assemblage as a meso-density fraction (1.8–2.4 g cm^{-3}; MF) from particulate OM as a low-density fraction (< 1.8 g cm^{-3}; LF) and crushed rock as a high-density fraction (> 2.4 g cm^{-3}; HF) using sodium polytungstate (SPT-0 grade, TC-Tungsten Compounds GmbH, D-96271 Grub am Forst, Germany), as described in Wagai et al. (2015). Briefly, 10.0 g of the mineral-OM mixture was mixed with 30 mL of sodium polytungstate with a final density of 1.8 g cm^{-3} and shaken at 120 rpm for 30 min. The suspension was then centrifuged at 2330 *g* for 20 min, and the floating material was collected on a 0.45 µm membrane filter. These steps were repeated at least three times to maximize the recovery. The material on the filter was washed with deionized water until the electric conductivity was below 50 mS cm^{-1}; this operation produced the LF fraction. The residue was resuspended in SPT solution adjusted to 2.4 g cm^{-3} at the sample: extractant ratio of 10 g:30 mL, shaken, and centrifugated. The floating material (1.8–2.4 g cm^{-3}) was transferred to a 250 mL centrifuge bottle, mixed with deionized water, and centrifuged at 17,000 *g* for 20 min. The supernatant was decanted, and this rinsing step was repeated until the electric conductivity of the supernatant became < 50 mS cm^{-1}. The final material was recovered as the MF fraction of 1.8–2.4 g cm^{-3}. The remaining residue (> 2.4 g cm^{-3}) was rinsed with deionized water in the same way as above to isolate the HF fraction of > 2.4 g cm^{-3}. Recovered LF was oven-dried at 80 °C, and MF and HF were freeze-dried.

2.4 Chemical analyses of the mixtures

Total C and N contents in the density fraction were determined by an elemental analyzer (vario MAX cube, Elementar Analysensysteme GmbH, Langenselbold, Germany). The C and N isotopic compositions of the initial leaf compost and the density fractions under the two basalt treatments after the incubation were analyzed on the continuous-flow stable isotope mass spectrometer (Delta V Advantage, Thermo Fisher Scientific Inc., USA) coupled with an elemental analyzer (Flash EA 1112 Series). To minimize the N blank, a gas-tight automatic sampler was used (Zero Blank Autosampler, Costech Analytical Technologies Inc., USA). To increase the sensitivity for analyzing the N isotopes, the combustion and reduction tubes (both 18 mm outer diameters) were exchanged with thinner ones (18–10 mm and 10–6 mm outer diameters, respectively; Ogawa et al., 2010; Koba et al., 2021). The obtained $^{13}C/^{12}C$ and $^{15}N/^{14}N$ ratios are shown in terms of the δ value ($\delta^{13}C$ and $\delta^{15}N$) relative to Vienna Pee Dee Belemnite and the air dinitrogen, respectively. Their analytical precisions are ± 0.2‰ except for the $\delta^{15}N$ values of the HF (± 0.4‰).

Extractable Al, Fe, Si, and Ca in the density fraction and bulk samples were quantified by the sequential extraction with sodium pyrophosphate (PP), oxalate-extractable (OX), and dithionite-extractable (DC), as described in Wagai et al. (2018). These extractions have been widely used as a practical method to estimate the concentration of organo-metal complexes, short-range-ordered minerals, and pedogenic Fe oxides, respectively (Shang and Tiessen, 1998; Heckman et al., 2018; Ashida et al., 2021; Hall and Thompson, 2022). However, cautions are required for their interpretation due to the limited selectivity in extracting target phases as discussed previously (Wagai et al., 2013b; Rennert, 2019; Fukumasu et al., 2025).

https://doi.org/10.5194/egusphere-2025-2840
Preprint. Discussion started: 10 July 2025

Briefly, each sample was extracted with 0.1 M sodium pyrophosphate (pH 10) at a sample: extractant ratio of 0.1 g:10 mL at 120 rpm for 16 h at room temperature, followed by high-speed centrifugation at 29,000 *g* for 40 min. After collecting an aliquot of the extract (approximately 7 mL) and discarding the remaining supernatant, the residue was extracted with 10 mL of 0.2 M acidified sodium oxalate solution (pH 3) at 150 rpm for 4 h at 25 °C in the dark and centrifuged in the same way. After collecting an aliquot of the extract and discarding the remaining supernatant, the residue was added 0.167 g of sodium dithionite and then extracted with 10 mL of 0.646 M sodium citrate at 120 rpm for 16 h at room temperature and centrifuged in the same way.

The amounts of Al, Fe, Si, and base cations (Na, Ca, K, and Mg) after each of the three extractions were measured by an inductively coupled plasma optical emission spectrometer (700 series ICP-OES, Agilent Technologies, Inc., CA, United States). The combined leachate from the eight wet-and-dry cycles from each column was also analyzed in the same way. The leachate was also analyzed for DOC by a TOC analyzer (TOC-L, Shimadzu, Kyoto, Japan) using non-pergeable organic C mode and for pH.

The pH of the bulk samples after the incubation was measured using a glass electrode in ultra-pure water (0.4 g: 4 mL) after 1 h of shaking at 150 rpm. Subsequently, we added 1.6 mL of 3.5 M KCl to the water suspension to measure pH in the 1 M KCl condition.

2.5 Imaging analyses of selected samples

Microscopic observation of the initial crushed rocks (granite, coarse basalt, and fine basalt) as well as the MF of their mixtures after the incubation was done using a scanning electron microscope (SU1510, Hitachi High-Tech Corporation, Tokyo, Japan). The subsets of MFs (stored in a suspension at ca 5 °C after the density fractionation without freeze-drying) were diluted in ultra-pure water and deposited on a carbon tape, air-dried, and coated with palladium before the observation.

The subsets of MF from selected treatments (granite and coarse basalt) using scanning transmission X-ray microscopy (STXM) and near-edge X-ray absorption fine structure (NEXAFS) to assess the spatial arrangement of key elements (C, Al, and Fe) and C structure within the shaking-resistant microaggregates present in MF. Another subsets of MF in suspension were diluted with ultra-pure water and weakly sonicated (< 10 J mL^{-1}) followed by deposition on a Si_3N_4 window (50 nm thick, window size 500 µm). To minimize the re-aggregation on the Si_3N_4 window upon drying, the samples were slowly dried at room temperature. Carbon, Al, and Fe were recorded by a compact STXM at BL-19A beamline in the Photon Factory of the High Energy Accelerator Research Organization, Ibaraki, Japan (Takeichi et al., 2016). The STXM data analysis was carried out with the IDL package aXis 2000 (Hitchcock, 2023). The distribution maps of C, Al, and Fe were obtained by subtracting the post-edge optical density (OD) image from the pre-edge OD image, respectively. Specifically, we collected images in the X-ray energy region of 280.0 and 300.0 eV for C K-edge adsorption, 700 and 709.5 eV for Fe L-edge adsorption, and 1550.0 and 1567.0 eV for Al K-edge adsorption (Solomon et al., 2012). The spatial resolution of the images was 200 nm.

2.6 Microbial community analyses

We also assessed the changes in bacterial community 16S amplicon sequencing using the initial leaf compost (n = 3), bulk samples from all four treatments on Day 55 (n = 3), and MF from selected treatments (granite, coarse basalt, and fine basalt) on Day 55 (n = 1). The latter was a composite of three reps due to the limited mass recovery of MF. The DNA was extracted from 0.4 g of each sample under wet conditions by the FastDNA® SPIN Kit for Soil (MP Biomedicals, California, USA) according to the manufacturer's instructions with a few modifications. Quantitative PCR (qPCR) assays were conducted using the fluorescent dye SYBR Green (THUNDERBIRD Next SYBR qPCR mix, TOYOBO) by a QuantStudio 3.0 real-time PCR System (Applied Biosystems/Thermo Fisher Scientific). 16S rRNA genes quantified using the primer pairs Bact1369F/ProK1492R (Suzuki et al., 2000) for the V3-V4 region of the 16S rRNA. The PCR reactions for 16S rRNA

https://doi.org/10.5194/egusphere-2025-2840
Preprint. Discussion started: 10 July 2025

started with an initial denaturing step of 95 °C for 30 s, followed by 40 cycles at 95 °C for 5 s and 60 °C for 30 s. Melting curve analyses involved a denaturing step at 95 °C for 15 s, annealing at 65 °C for 1 min, and melting in 0.1 °C steps up to 95 °C. Standard curves for each assay were generated by serial dilutions of linearized plasmids with cloned fragments of environmental DNA. Amplification efficiencies were 96.4 %. 16S rRNA amplicon sequencing and subsequent bioinformatics analysis are the same as the previous studies (Bamba et al., 2024; Hara et al., 2024). DNA sequencing data (16S rRNA gene amplicon) are available at the NCBI Sequence Read Archive (SRA) under BioProject ID PRJDB18777. For the 16S rRNA amplicon, taxonomy was assigned to ASVs using the SINTAX algorithm (Edgar, 2016) implemented in USEARCH (v11.0.667) against the RDP database v18 (Cole et al., 2014).

2.7 Statistics and calculations

The effect of mineral type on the measured variables was tested by one-way ANOVA. The changes in the variables over the incubation duration were examined by a *t*-test. All statistical analyses were performed in Microsoft Excel for Microsoft 365 MSO and Excel Toukei (BellCurve for Excel, Social Survey Research Information, Tokyo, Japan).

We estimated the total amounts of C and N in the mineral-OM mixtures after the incubation by summing up the C and N in LF, MF, and HF instead of the bulk sample values because we expected less sub-sampling error from the former. Specifically, roughly 44% of the mass of the incubated mixture was used for the density fractionation analysis, whereas only 13% was allocated for bulk sample C and N analysis. We estimated the total amounts of the extractable metals in the same way. The high mass recovery of the density fractions (range: 99–101%, Table 1) justified this approach.

Table 1. Recovery of mass, C, N, and extractable Al, Fe, and Si after the density fractionation of the mineral-OM mixtures on Day 55.

	Mass (%)	C (%)	N (%)	Extractable Al (%)	Extractable Fe (%)	Extractable Si (%)
Granite 38–75 µm	100 ± 0	95 ± 12	100 ± 6	N.A.	N.A.	N.A.
Basalt 38–75 µm	99 ± 1	86 ± 8	90 ± 8	88 ± 7	99 ± 6	85 ± 3
Basalt 20–38 µm	100 ± 0	102 ± 1	106 ± 1	95 ± 3	108 ± 1	93 ± 0
Sand 100–300 µm	101 ± 0	107 ± 14	109 ± 18	N.A.	N.A.	N.A.

Al and Fe were extracted sequentially with sodium pyrophosphate, acid oxalate, and dithionite-citrate.
Value shows mean ± standard deviation (n = 3).
N.A. Not analyzed due to limited mass recovery of MF.

Alpha and beta diversities of the bacterial communities in the initial leaf compost and post-incubation samples were calculated using the “phyloseq” pipeline (McMurdie and Holmes, 2013) and the “microeco” pipeline (Liu et al., 2021), respectively. Principal coordinate analysis (PCoA) of unweighted UniFrac distance was used to visualize beta diversity between the treatments. We estimated the influence of the mineral type in the mineral-OM mixtures on the beta diversity by permutational multivariate analysis of variance (PERMANOVA) using the ‘adonis’ function in the ‘vegan’ package (Oksanen, 2013). We further analyzed the correlations between the bacterial composition and the property variables of MF and bulk samples on Day 55 and initial compost by the Mantel test using the ‘mantel’ function in the ‘ecodist’ package (Goslee and Urban, 2007). All the microbial analyses were performed using R version 4.2.0 (www.r-project.org).

3 Results

3.1 Recovery after density fractionation

Density fractionation of the mineral-OM mixtures at the end of the 55-day incubation experiment showed reasonable

https://doi.org/10.5194/egusphere-2025-2840
Preprint. Discussion started: 10 July 2025

recoveries for all the mineral treatments: 99–101% for mass, 86–107% for C, 90–109% for N, 88–95% for extractable Al, 99–108% for extractable Fe, and 85–93% for extractable Si (Table 1). Some variations among the mineral treatments were found. The coarse basalt treatment had less complete C and N recoveries than the other treatments and less complete extractable Al and Si recoveries relative to the fine basalt treatment. Overall, we considered that these recoveries were at acceptable levels for further assessment of the elemental distribution patterns across the density fractions.

3.2 Mass, C and N, and $\delta^{13}C$ and $\delta^{15}N$

Mass proportion in MF after the incubation was the highest in the fine basalt (13%), followed by the coarse basalt (7.1%), granite (0.57%), and sand (0.17%) treatments (Fig. 2). The increases in MF largely corresponded to the reduction in the mass of HF. However, the initial granite, coarse basalt, and fine basalt contained small amounts of MF, accounting for 0.30%, 6.8%, and 6.3% of the initial mass of respective minerals (Fig. 3a). After accounting for the initial MF in these treatments, we detected a significant increase in the mass of MF after the incubation for the granite and fine basalt treatments (Fig. 3a). The largest increase in MF mass was found in the fine basalt treatment (65 mg g^{-1} bulk) whereas that in the coarse basalt and sand treatments changed little (0.26–3.0 mg g^{-1} bulk) over the 55-day duration.

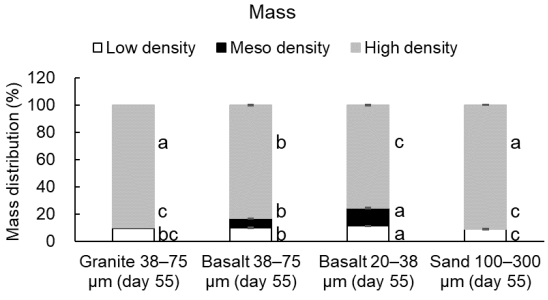

Figure 2. Mass distributions of the four mineral-OM mixtures across low-, meso-, and high-density fractions on Day 55. The same letters in each density fraction are not significantly different at $P < 0.05$ (Tukey's test; $n = 3$).

The C concentration in LF on Day 55 ranged from 378 to 431 mg g^{-1} fraction (data not shown) in comparison with the initial leaf compost (408 mg C g^{-1}). Carbon distribution in LF differed among the treatments in the following order: fine basalt > coarse basalt > granite > sand (Table S4). The same pattern was found for MF and HF. Because the initial crushed minerals contained only small amounts of MF mass (Fig. 3a) and essentially no C, the C increase in MF after the incubation was significant for all four treatments ($P < 0.01$, Fig. 3b). The largest increase was shown in the fine basalt (1.3 mg C g^{-1} bulk) followed by the coarse basalt (0.90 mg C g^{-1} bulk) and then the granite (0.55 mg C g^{-1} bulk) treatments. Even in the sand treatment, we detected a significant increase in the amount of C in MF (0.10 mg C g^{-1} bulk). When summing up the C and N in all three fractions, the total amounts of C and N left after the incubation showed a significant difference among the treatments in the following order: fine basalt > coarse basalt > granite > sand (Table S4).

The C:N ratio of the initial leaf compost and that of LF after the incubation were similar in all four treatments (Fig. 4a), as the majority of C was present in LF. When comparing the density fractions, the C:N ratio progressively declined with increasing density. In other words, the loss of OM from LF towards HF during the incubation was greater for C than N (Table S4). The values of $\delta^{13}C$ and $\delta^{15}N$ of the initial leaf compost and those of LF after the incubation were similar in both basalt treatments (Fig. 4b). The value of $\delta^{13}C$ significantly increased from LF towards HF, whereas $\delta^{15}N$ showed a significant increase from LF to MF and apparent decline from MF to HF (Fig. 4b).

https://doi.org/10.5194/egusphere-2025-2840
Preprint. Discussion started: 10 July 2025

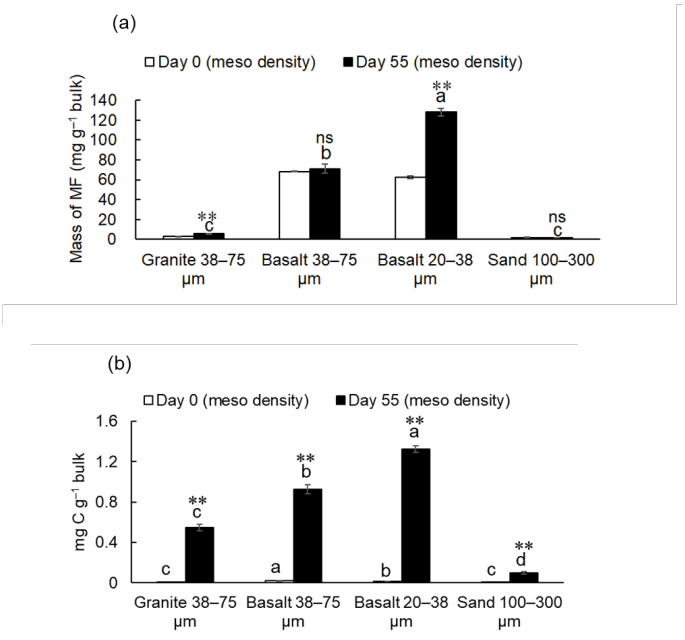

Figure 3. The mass of meso-density fraction (MF) in the mineral-OM mixtures before (Day 0) and after the incubation (Day 55) (a). The amounts of C in MF in the bulk mixtures on Day 0 and Day 55 (b). The same letters in each experimental day are not significantly different at $P < 0.05$ (Tukey's test; $n = 3$). Differences between the "on Day 0" and "on Day 55" in MF are significant at $^{**}P < 0.01$; ns, not significant (*t*-test).

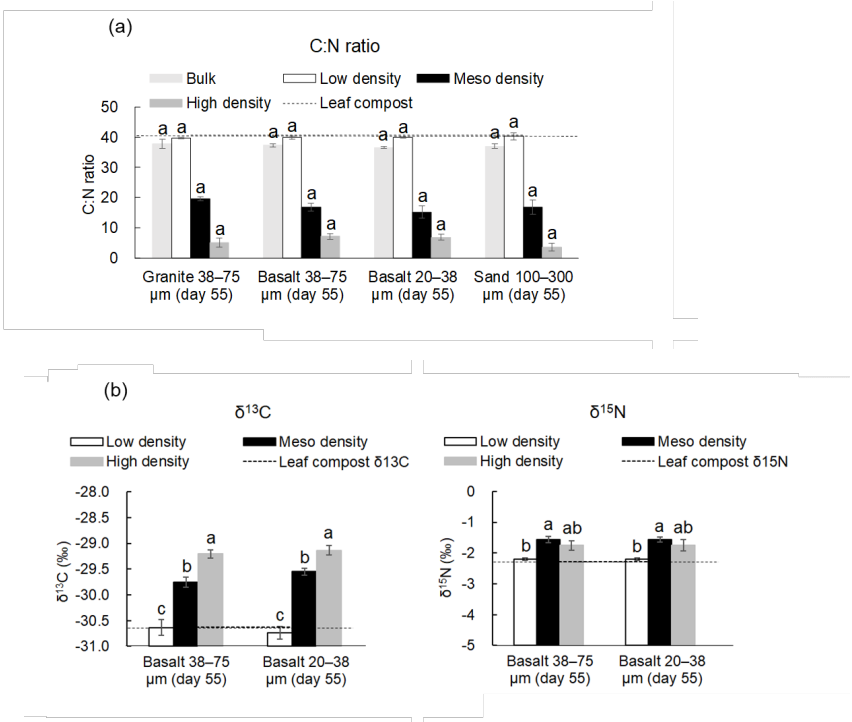

https://doi.org/10.5194/egusphere-2025-2840
Preprint. Discussion started: 10 July 2025

Figure 4. C:N ratio along density gradient in the mineral-OM mixtures on Day 55 (a), and values of $\delta^{13}C$ and $\delta^{15}N$ along density gradient of the two basalt treatments on Day 55 and in the leaf compost (b). The same letters in each bulk or density fraction are not significantly different at $P < 0.05$ (Tukey's test; $n = 3$).

3.3 Extractable Al, Fe, and Si and pH

The initial sand contained only negligible amounts of OX-extractable metals ($metal_{OX}$), and the initial granite contained < 1 mg g^{-1} bulk of $metal_{OX}$ (Table S2). The initial coarse and fine basalts had much higher extractable metals. Particularly, the initial fine basalt had a higher amount of PP-extractable Al, Fe, and Si (Al_{PP}, Fe_{PP}, Si_{PP}) as well as Al_{OX}, Fe_{OX}, and Si_{OX} compared to the initial coarse basalt. The higher extractable Al and Fe in the fine basalt may be explained in part by the slightly higher total contents of these metals, but that was not the case for Si (Table S1).

After the 55-day incubation, we detected some increases in the extractable metals in LF and in the MF from the two basalt treatments, where we were able to recover enough masses of MF (Table 2; Table S5-1; Table S5-2; Table S6; Fig. 2). No extraction from MF was possible for the granite and sand treatments due to the very low mass recovery (Fig. 2). The total extractable metals, from the sequential PP, OX, and DC extractions, in LF+MF in the coarse basalt and fine basalt treatments increased from 1.1–1.3 to 1.4–3.1 mg g^{-1} bulk for Al and from 3.9–4.5 to 5.4–13 mg g^{-1} bulk for Fe during the 55-day incubation (Table S5-2; Table S6). In HF, on the other hand, the total extractable Al slightly decreased from 5.1–6.0 to 3.7–4.1 mg g^{-1} bulk, and that of Fe decreased from 34–36 to 25–29 mg g^{-1} bulk during the incubation. The LF isolated after the incubation contained low amounts of extractable Al, Fe, and Si with some variations among the treatments (Table S6). Higher concentrations of extractable Al and Fe in LF and HF were found in the two basalt treatments compared to the granite and sand treatments. When summing up the total extractable Al, Fe, and Si among the three fractions, the significant increase over the incubation period was detected only for Al (1.49 ± 0.25) and Fe (5.10 ± 1.78 mg g^{-1} bulk) from the fine basalt treatment. Thus, the observed changes in the extractable metals among the fractions resulted from both chemical weathering and redistribution for the fine basalt and only from redistribution for the other treatments.

Table 2. Concentrations (per fraction) of extractable Al, Fe, and Si in each density fraction from the mineral-OM mixtures on Day 55.

	Sodium pyrophosphate (PP)			Acid oxalate (OX)			Dithionite-citrate (DC)		
	Al (mg g^{-1} fraction)	Fe (mg g^{-1} fraction)	Si (mg g^{-1} fraction)	Al (mg g^{-1} fraction)	Fe (mg g^{-1} fraction)	Si (mg g^{-1} fraction)	Al (mg g^{-1} fraction)	Fe (mg g^{-1} fraction)	Si (mg g^{-1} fraction)
Low-density fraction (< 1.8 g cm^{-3})									
Granite 38–75 µm	0.33 ± 0.03	0.25 ± 0.00	3.0 ± 0.1	1.0 ± 0.0	1.7 ± 0.0	0.51 ± 0.01	0.30 ± 0.03	1.5 ± 0.1	2.7 ± 0.2
Basalt 38–75 µm	0.48 ± 0.01	0.53 ± 0.02	2.0 ± 0.1	1.4 ± 0.1	3.3 ± 0.1	0.67 ± 0.02	0.37 ± 0.01	2.1 ± 0.0	4.0 ± 0.1
Basalt 20–38 µm	0.52 ± 0.02	0.71 ± 0.02	1.6 ± 0.0	2.0 ± 0.1	6.3 ± 0.1	1.2 ± 0.0	0.48 ± 0.01	3.3 ± 0.1	6.4 ± 0.1
Sand 100–300 µm	0.39 ± 0.01	0.24 ± 0.00	3.1 ± 0.2	1.1 ± 0.1	1.6 ± 0.0	0.49 ± 0.03	0.26 ± 0.04	1.1 ± 0.1	2.4 ± 0.3
Meso-density fraction (1.8–2.4 g cm^{-3})									
Granite 38–75 µm	N.A.	N.A.	N.A.	N.A.	N.A.	N.A.	N.A.	N.A.	N.A.
Basalt 38–75 µm	0.44 ± 0.01	0.76 ± 0.04	1.7 ± 0.0	13 ± 3	51 ± 11	6.1 ± 1.3	2.7 ± 0.1	16 ± 1	9.6 ± 0.2
Basalt 20–38 µm	0.44 ± 0.00	0.69 ± 0.02	1.7 ± 0.0	18 ± 1	74 ± 1	9.4 ± 0.2	2.4 ± 0.1	14 ± 0	9.2 ± 0.1
Sand 100–300 µm	N.A.	N.A.	N.A.	N.A.	N.A.	N.A.	N.A.	N.A.	N.A.
High-density fraction (> 2.4 g cm^{-3})									
Granite 38–75 µm	0.0 ± 0.0	0.0 ± 0.0	0.0 ± 0.0	0.12 ± 0.02	0.68 ± 0.04	0.13 ± 0.02	0.18 ± 0.01	1.8 ± 0.0	0.73 ± 0.02
Basalt 38–75 µm	0.071 ± 0.011	0.23 ± 0.01	0.36 ± 0.02	3.7 ± 0.1	25 ± 1	2.2 ± 0.1	0.72 ± 0.04	4.8 ± 0.3	8.9 ± 0.2
Basalt 20–38 µm	0.15 ± 0.00	0.28 ± 0.00	0.57 ± 0.02	4.7 ± 0.1	34 ± 1	3.1 ± 0.0	0.59 ± 0.05	4.9 ± 0.6	9.2 ± 0.1
Sand 100–300 µm	0.0 ± 0.0	0.0 ± 0.0	0.0 ± 0.0	0.015 ± 0.008	0.14 ± 0.10	0.0 ± 0.0	0.087 ± 0.014	1.3 ± 0.3	0.080 ± 0.021

Al, Fe, and Si were extracted sequentially with sodium pyrophosphate, acid oxalate, and dithionite-citrate.

Value shows mean ± standard deviation (n = 3).

N.A. Not analyzed due to limited mass recovery of MF.

https://doi.org/10.5194/egusphere-2025-2840
Preprint. Discussion started: 10 July 2025

When focusing on MF, statistically detectable increase (thus accumulation) of extractable metals and metalloid during the incubation was found only for the fine basalt treatment (Fig. 5). For the two basalt treatments, the amounts of Al_{OX} and Fe_{OX} in MF on Day 55 accounted for 82–87% and 76–83% of the total extractable metal pools (i.e., the sum of PP, OX, and DC extractions), respectively (Table S6). The fine basalt treatment significantly increased the amounts of Al, Fe, and Si in MF for all three extractable phases during the incubation ($P < 0.05$) (Fig. 5). On the other hand, the coarse basalt treatment showed a small but significant increase in Al_{PP} in MF during the incubation ($P < 0.01$, Fig. 5a). The fine basalt treatment had significantly higher amounts of extractable Al, Fe, and Si in MF than the coarse basalt treatment for all extractable phases on Day 55 ($P < 0.05$, Fig. 5; Table S6). In addition, the amount of extractable Ca in MF also showed a significant increase for PP and DC extractable phases in both basalt treatments during the incubation ($P < 0.01$, Fig. S3). Note that we did not detect OX-extractable Ca, presumably due to the precipitation of calcium oxalate. The interpretation of extractable Ca in the current study needs some caution.

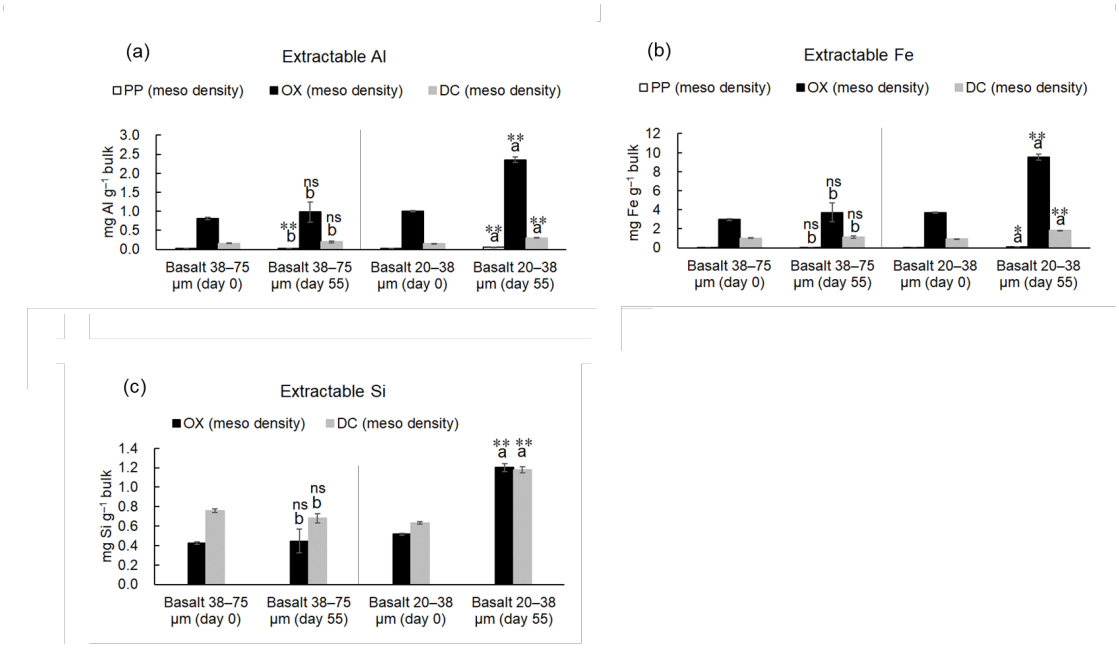

Figure 5. Amounts of extractable Al (a), Fe (b), and Si (c) in MF from the mineral-OM mixtures on Day 0 and Day 55. The extractions were done sequentially with sodium pyrophosphate (PP), acid oxalate (OX), and dithionite-citrate (DC). The same letters in each extraction (i.e., PP, OX, or DC) on Day 55 are not significantly different at $P < 0.05$ (Tukey's test; $n = 3$). Differences between the "on Day 0" and "on Day 55" in each mineral-OM mixture and each extraction (i.e., PP, OX, or DC) are significant at $*P < 0.05$, $**P < 0.01$; ns, not significant (*t*-test).

We further assessed the stoichiometry of the major elements accumulated in MF during the incubation. The carbon-to-extractable metal ratios in moles ranged from 0.5 to 2.3, and C was enriched for Fe than Al in both basalt treatments (Table S7). Over the 55-day incubation, we detected significant enrichment of Fe_{OX} for both basalt treatments and that of Al_{OX} for the coarse basalt treatment relative to Si_{OX} (Table 3). Moreover, the Fe_{OX}:Al_{OX} ratio showed a significant increase in the fine basalt treatment.

The pH(H_2O) of the bulk samples of all treatments on Day 55 ranged between 6.5 and 7.6, with the highest pH in the fine basalt treatment, followed by the coarse basalt, while the granite and sand treatments were slightly acidic (Table 4). The difference in pH(KCl) among the treatments was less clear.

https://doi.org/10.5194/egusphere-2025-2840
Preprint. Discussion started: 10 July 2025

Table 3. Molar ratios of acid oxalate extractable Al, Fe, and Si in MF in the two basalt treatments before and after the 55-day incubation.

		Meso-density fraction (1.8–2.4 g cm^{-3})								
		Al:Si			Fe:Si			Fe:Al		
Basalt 38–75 µm	Day 0	2.0	± 0.0		3.5	± 0.0		1.8	± 0.0	
	Day 55	2.3	± 0.0	**	4.2	± 0.1	**	1.8	± 0.0	ns
Basalt 20–38 µm	Day 0	2.0	± 0.0		3.6	± 0.0		1.8	± 0.0	
	Day 55	2.0	± 0.0	ns	4.0	± 0.0	**	2.0	± 0.0	**

Value shows mean ± standard deviation (n = 3).
Differences between the "on Day 0" and "on Day 55" in each treatment are significant at **P < 0.01; ns, not significant (t-test).

Table 4. pH in the mineral-OM mixtures after the 55-day incubation.

	pH(H_2O)			pH(KCl)		
Granite 38–75 µm	6.7	± 0.0	c	6.1	± 0.0	a
Basalt 38–75 µm	7.3	± 0.0	b	5.9	± 0.0	bc
Basalt 20–38 µm	7.6	± 0.0	a	6.0	± 0.0	ab
Sand 100–300 µm	6.5	± 0.0	d	5.8	± 0.0	c

Value shows mean ± standard deviation (n = 3).
Means followed by the same letter are not significantly different at P < 0.05 (Tukey's test; n = 3).

3.4 Leaching loss of elements and leachate chemistry

The total amount of DOC released from the mineral-OM mixtures during the eight repeated leaching events was 13–15 mg C per incubation column (Table 5), which was equivalent to 1.3–1.5% of the total C in the initial mixtures. No significant difference in DOC release was found among the four treatments. For the major rock-forming elements, Fe leaching was the highest in the fine basalt, followed by the coarse basalt treatment, and Si leaching showed similar patterns (Table 5). Conversely, the total amount of Al leached was the highest in the sand and the lowest in the coarse basalt treatment. The sum of base cations leached was the highest in the fine basalt treatment, followed by the coarse basalt, sand, and granite treatments. The type of base cation leached during the incubation showed the following order: Ca > Na > K > Mg. The pH of the leachates was neutral to alkaline (7.1–9.1), with the highest pH in the fine basalt, followed by the coarse basalt treatment, while the other two treatments had nearly neutral pH (Table 4). The observed pH difference largely corresponded to the variation of the leachate chemistry among the treatments (e.g., Na, Ca, and Al).

Table 5. Amounts of DOC, Al, Fe, Si, base cations, and pH in leachates released from the mineral-OM mixtures during the 55-day incubation (the sum of the eight repeated leaching events).

	DOC (mg)			Al (mg)			Fe (mg)			Si (mg)		
Granite 38–75 µm	14	± 1	a	0.0068	± 0.0019	ab	0.015	± 0.001	c	1.5	± 0.1	b
Basalt 38–75 µm	13	± 0	a	0.0044	± 0.0007	b	0.028	± 0.001	b	3.5	± 0.0	a
Basalt 20–38 µm	15	± 0	a	0.0060	± 0.0009	ab	0.036	± 0.000	A	4.5	± 0.2	a
Sand 100–300 µm	13	± 1	a	0.010	± 0.001	a	0.013	± 0.000	C	1.7	± 0.4	b

https://doi.org/10.5194/egusphere-2025-2840
Preprint. Discussion started: 10 July 2025

	Sum of base cations (mg)			Na (mg)		Ca (mg)		K (mg)		Mg (mg)		pH		
Granite 38–75 µm	7.7	± 0.3	c	1.6	± 0.0	4.2	± 0.2	0.94	± 0.06	1.0	± 0.1	7.2	± 0.0	c
Basalt 38–75 µm	9.8	± 0.3	b	2.0	± 0.1	5.5	± 0.2	1.7	± 0.0	0.62	± 0.04	7.9	± 0.1	b
Basalt 20–38 µm	14	± 0	a	6.1	± 0.2	5.4	± 0.1	1.6	± 0.0	0.49	± 0.02	9.1	± 0.0	a
Sand 100–300 µm	8.9	± 0.7	bc	1.2	± 0.2	3.3	± 0.4	3.3	± 0.3	1.1	± 0.1	7.1	± 0.1	c

Value shows mean ± standard deviation (n = 3).

Means followed by the same letter are not significantly different at $P < 0.05$ (Tukey's test; n = 3).

3.5 Microscopic observations of organo-mineral assemblage by SEM and STXM-NEXAFS

We observed some shaking-resistant, organo-mineral assemblages in the post-incubation MF (Fig. 6). The observed assemblages were present as microaggregates of 100–200 µm in diameter, consisting of crushed rocks (Fig. 6b, 6d, 6f) and OM, including fungal hyphae (Fig. 6d). Greater aggregate sizes were apparent in the two basalt treatments compared to the granite treatment (Fig. 6d, 6f). Much finer subunits (rock fragments) were confirmed in the fine basalt aggregates compared to the coarse basalt aggregates.

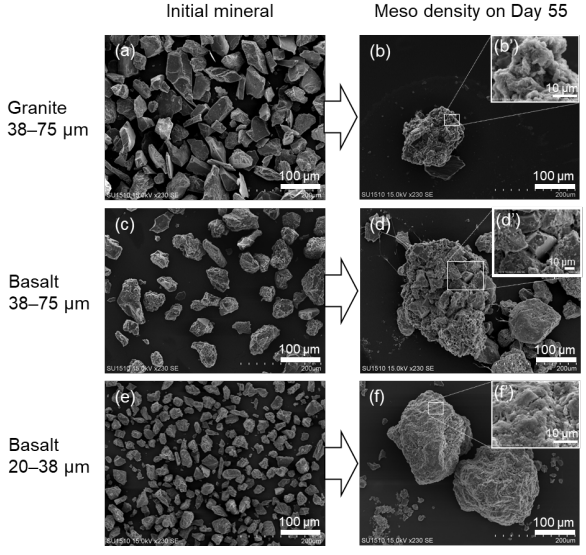

Figure 6. SEM images of the crushed rock minerals and the isolated density fraction. (a) initial granite mineral, (b) MF of granite, (c) initial coarse basalt mineral, (d) MF of coarse basalt, (e) initial fine basalt mineral, and (f) MF of fine basalt.

The subsamples of dispersed MF material from the selected mineral-OM mixtures, the granite and coarse basalt treatments (see Fig. S4 for SEM images), were further characterized to assess the chemical nature of the organo-mineral assemblages by STXM-NEXAFS (Fig. 7). We first obtained the spatial distribution of C, Al, and Fe for a large area (35 × 35 µm, Fig. 7A, 7B). As the C-rich zones in the targeted assemblage were patchy, we selected one of these patches and the adjacent mineral-rich zones as a focused area (5 × 5 µm) to examine the distribution of C functional groups (Fig. 7a, 7b). The submicron spatial heterogeneity was present for C within the 5 × 5 µm areas. In the granite sample, the C-rich zone (shown as ROI in Fig. 7a) was relatively enriched in aromatic and, to a lesser extent, carboxylic C compared to the average C K-

https://doi.org/10.5194/egusphere-2025-2840
Preprint. Discussion started: 10 July 2025

edge NEXAFS spectra of the whole 5 × 5 µm area (Fig. 7a1, 7a3). The spatial distribution of the two C functional groups was similar (Fig. 7a1, 7a3). While some overlaps of C with Fe and Al (Fig. 7a4, 7a5) were shown, the metal-rich patches appeared to be present adjacent to, rather than overlapped with, the C-rich zone. The dominance of Fe over Al shown in the fine basalt treatment (Fig. 7B) was in line with the higher content and increase of Fe_{OX} relative to Al_{OX} phase (Fig. 5a, 5b). In the coarse basalt sample, by contrast, the C-rich zone (ROI in Fig. 7b) was enriched in ketonic C compared to the average C of the whole area (Fig. 7b2). Aromatic C and carboxylic C appeared to be distributed separately (Fig. 7b1, 7b3). The distributions of Fe and Al were not successfully measured. While the three major C peaks were found in MF of both granite and coarse basalt treatments, the latter appeared to have a higher relative abundance of ketonic C (Fig. 7, middle left spectra).

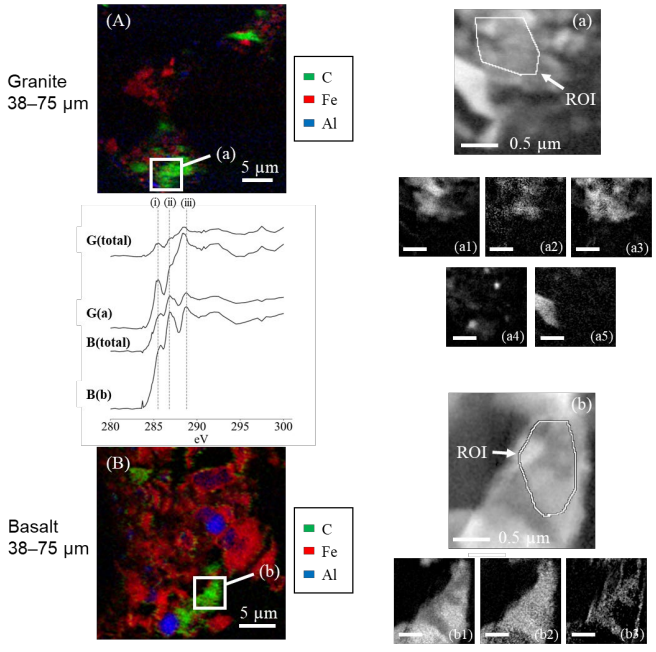

Figure 7. The elemental maps obtained with STXM-NEXAFS analysis. The images show the distribution of elements in the 35 x 35 µm region of interest for MF of granite (A) and coarse basalt treatments (B) after the 55-day incubation, respectively. The images (a) and (b) show the C optical density for a selected C-rich region at a higher resolution (5 x 5 µm). The C K-edge NEXAFS spectra at middle left panel show the image stacks for the total 35 x 35 µm region of granite, G(total), and that of coarse basalt, B(total), and for the C-rich region spectra of granite, G(a), and coarse basalt, B(b). The dashed lines (i), (ii), and (iii) represent the energies at 285.5, 286.8, and 288.8 eV corresponding to aromatic C, ketonic C, and carboxylic C. The images (a1), (a2), and (a3) and (b1), (b2), and (b3) show the spatial distribution of specific C type, aromatic C, ketonic C, and carboxyl C, respectively, in a 5 x 5 µm region. The image (a4) and (a5) shows the spatial distribution of Fe and Al in the same area corresponding to the image (a).

3.6 Bacterial community composition after the 55-day incubation

We assessed the effect of the mineral treatment on the microbial community composition at the end of the incubation using bacterial amplicon sequencing. The bacterial copy number ranged from 3.7 x 10^8 to 1.5 x 10^9, and the initial compost tended to have a higher number than the bulk samples after the incubation (Table S8). Among the post-incubation bulk samples, the bacterial number decreased in the following order: sand > granite > two basalt treatments, with no significant difference among the treatments (ANOVA, $P = 0.08$). The alpha diversity indices, including Chao1, Shannon index, and evenness showed no significant differences among the treatments (Table S8; ANOVA, $P = 0.28$, 0.24, 0.10, respectively). Yet the beta

https://doi.org/10.5194/egusphere-2025-2840
Preprint. Discussion started: 10 July 2025

diversity (PCoA plot; Fig. 8a) was different among the treatments (PERMANOVA, F =5.63, P = 0.001). The sum of the relative abundance of the three ASVs belonging to Neobacillus, the most dominant genus, was higher in MF compared to the bulk sample (15.5 ±8.4 % and 3.5 ±1.7 %, respectively, t-test, P = 0.0036). The mantel results using the data of MF and the bulk samples on Day 55 further showed significant correlations between the microbial composition (PCoA score) and selected soil properties including total C, total N, pH(KCl), pH(H_2O), Fe_{PP}, and Al_{PP} (R^2 = 0.86, 0.86, 0.82, 0.80, 0.30 and 0.22 respectively, P < 0.05; Table S9).

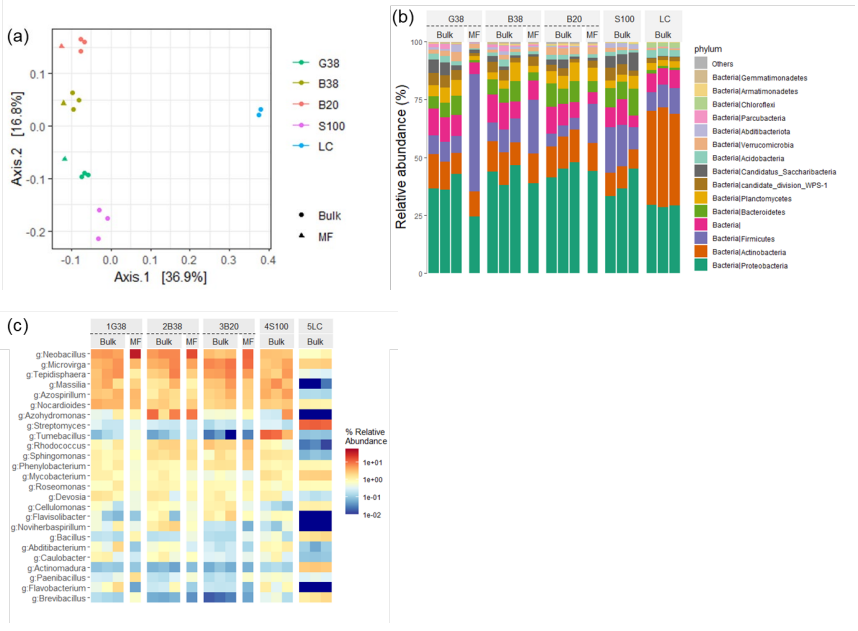

Figure 8. Beta diversity shown by PCoA plot based on 16S rRNA gene (a), bar plot at phylum level (b), and heatmap at genus level (c) in bulk and MF samples. G38: granite 38–75 µm (day 55), B38: basalt 38–75 µm (day 55), B20: basalt 20–38 µm (day 55), S100: sand 100–300 µm (day 55), and LC: initial leaf compost.

4 Discussion

4.1 Testing of the organo-metallic glue hypothesis

We designed the simple incubation experiment to mimic key aspects of field soil conditions, namely wet-dry cycles with water percolation and microbial heterotrophic activity, and quantified the formation of organo-mineral assemblage as meso-density fraction (MF), along with associated changes in both OM and rock-forming elements. Among the three crushed rocks used, the most weatherable treatment, the fine basalt-OM mixture, showed the most significant increase in the mass (Fig. 3a) and C (Fig. 3b), and extractable metals and metalloid (esp. Fe_{OX}, Al_{OX}, and Si_{OX}, Fig. 5) in MF. When normalizing to the rock added, the accretion of C as organo-mineral assemblage (i.e., in MF) during the 55-day incubation experiment was 1.49 ± 0.06 (fine basalt), 1.04 ± 0.08 (coarse basalt), and 0.62 ± 0.06 (granite) mg C g^{-1} rock. While the formation of mineral-associated OM (MAOM) co-occurred with the accretion of extractable metals, these rock-forming elements could come from two sources – inherent extractable metals (e.g., secondary minerals present in the crushed basalt) and weathering-derived metals during the incubation. In the fine basalt where significant increases in extractable Al and Fe were found on a bulk basis (section 3.3), we estimated that up to 62% of Al and 50% of Fe accreted in MF derived from the basalt weathering during the experiment while the rest resulted from the redistribution/transfer from HF (i.e., preferential metal enrichment in MF). While co-localization of OM and pedogenic metal phases in various MAOM fractions has been shown across a range

https://doi.org/10.5194/egusphere-2025-2840
Preprint. Discussion started: 10 July 2025

of soils (Wagai et al., 2020 and the reference therein), the formation rate of organo-mineral assemblage or the metal source remained unclear. The fine basalt treatment in the current experiment demonstrated the rapid assemblage formation and its direct linkage to weathering-derived metal supply, supporting the organo-metallic glue hypothesis.

Multiple lines of evidence point to the preferential accretion of microbially-processed, N-rich OM during the organo-mineral assemblage formation. First, the C:N ratio of OM in MF sample was significantly lower than that in LF in all four mineral-OM mixtures on Day 55 (Fig. 4a). Second, MF sample had higher $\delta^{13}C$ and $\delta^{15}N$ by 0.88–1.2‰ and 0.63–0.64‰ relative to LF, respectively, for both basalt treatments (Fig. 4b). The negative $\delta^{15}N$ values observed are within the common range for temperate forest leaves (−2.8 ± 2.0‰; Martinelli et al., 1999) and for organic layers of forest soils in temperate climate zone (–0.3 ± 0.3‰; Choi et al., 2020), which likely reflects the fact that the OM used in our study derived from tree leaves. Leaf compost itself contains a variety of plant- and microbially-derived compounds. Thus, the observed variation in OM chemistry among the fractions cannot be fully attributed to the reactions that took place during the 55-day incubation period. Our results are, nonetheless, consistent with the previous density fractionation studies that showed $\delta^{15}N$ increases with increasing soil particle density (Sollins et al., 2009; Hatton et al., 2012; Moni et al., 2012). Interestingly, while at very low C concentration (Table S4), OM in HF had similar or greater microbial signatures compared to OM in MF (Fig. 4b). These results imply that MF likely entrapped less-microbially-processed OM (e.g., decaying POM fragments) due presumably to the gluing effect of organo-metal coprecipitates whereas OM in HF is stabilized largely via adsorption on the crushed rock surfaces, as illustrated in the conceptual model previously (Wagai et al., 2020). Our results are also in line with the direct evidence that N-rich OM was preferentially bound to the mineral surface at the single-digit nanometer scale in an Andisol (Possinger et al., 2020). Third, the STXM-NEXAFS analysis (Fig. 7) further demonstrated that the C spectra of MF were comparable to those of soil OM (Solomon et al., 2012; Chen et al., 2014; Prietzel et al., 2018), which is dominated by microbially-processed OM in mineral soils (Sollins et al., 2009; Heckman et al., 2022). Our incubation condition (repeated wet-and-dry cycles and inoculation at each cycle) might have promoted the supply and turnover of microbial cell debris (Krause et al., 2019).

The formation of organo-mineral assemblage from the basalt-derived mixtures, along with the preferential accumulation of N-rich OM in MF, indicates a connection between microbial heterotrophic activity, chemical weathering, and aggregation. Microbes directly and indirectly promote rock and mineral weathering via mineral disaggregation, hydration, and dissolution (Banfield et al., 1999; Burghelea et al., 2015; Finlay et al., 2020). Metals released by weathering may precipitate on the surface of cells or biofilms as low-crystallinity Al and Fe oxides and silicates (Lybrand et al., 2019) that are mostly extractable by the acid oxalate method. In our study, more C was retained in MF under the treatments with higher reactive metal concentrations (Fig. 3b; Fig. 5), suggesting that the heterotrophic activity might have slowed down due to the higher abundance of reactive metals, slightly higher pH (Table 4), and greater aggregate formation (Fig. 3a). The microbial community was significantly different among the treatments on Day 55 especially between the two basalts and the other two treatments (Fig. 8) while the bacterial copy number and species richness remained similar (Table S8). We noted that the most abundant genus found in the studied samples, *Neobacillus*, was more enriched in MF compared to the bulk fraction, regardless of the treatments (Fig. 8c). To the extent that this genus tends to have biomineralization attributes (Farda et al., 2022; Bhattacharjee et al., 2023), our 16S amplicon results support the idea that MF is a hotspot of intimate microbe-mineral interaction (e.g., mineralosphere, Uroz et al., 2015).

4.2 Chemistry of the organo-mineral assemblage formed

We further assessed the nature of organo-mineral assemblage based on the chemical composition of MF formed during the 55-day incubation experiment. For the two basalt treatments, the C-to-metal (Fe+Al) ratio in MF was calculated by accounting for the extractable metals present in the initial rocks. When summing up the three extractions for metal, the C:metal ratio was 0.36 ± 0.01 and 0.64 ± 0.21 (mol:mol) for the fine and coarse basalt, respectively. The observed ratios

https://doi.org/10.5194/egusphere-2025-2840
Preprint. Discussion started: 10 July 2025

were within the range found in the coprecipitates formed between low-molecular-weight OM and rock-derived metals and metalloids in solution (Tamrat et al., 2019; Jamoteau et al., 2023) and lower than the typical ratios reported for the organo-metal complexes in Andisols and spodic horizon (Takahashi and Dahlgren, 2016; Lundström et al., 2000). In our experiment, the formation of the pedogenic metal phase mainly occurred as the Fe_{OX} phase (Fig. 5b). Assuming ferrihydrite for this phase, the accreted OM in MF was equivalent to 68.2 ± 1.3 mg C g^{-1} oxide. This value is comparable to the maximum sorptive capacity of ferrihydrite under laboratory conditions (Tipping, 1981; Kaiser et al., 1997). In theory, sorption alone could account for the observed levels of OM; however, coprecipitation, which includes sorptive associations, cannot be excluded. Based on these considerations, we propose that the organo-metal associations formed in MF under the basalt treatments are best characterized as organo-metal coprecipitates in which accreted OM exists both as adsorptive associations with Fe-rich secondary mineral phase (e.g., Wagai and Mayer, 2007) and as complexes with released metal cations and metalloids (e.g., Jamoteau et al., 2023).

Further assessment of the stoichiometric relationship gave hints on the nature of the organo-metal coprecipitates found in MF. First, roughly two orders of magnitude higher formation of Fe_{OX} and Al_{OX} phases compared to Fe_{PP} and Al_{PP} phases in MF under the basalt treatments (Table S6) may suggest a greater role of adsorptive association relative to organo-metal complexation. The direct micro-scale observation of a focused region of MF aggregate in the coarse basalt treatment (Fig. 7B) showed Fe dominance with the patchy distribution of Al and C (largely ketonic), implying the major metal phase formed (i.e., Fe_{ox} phase, Fig. 5b) might have entrapped a glob of OM. However, our observed regions were very limited, and generalization is not possible. Second, in both basalt treatments, MF was significantly enriched in Fe_{OX} and Al_{OX} relative to Si_{OX} after the incubation, except for the fine basalt treatment where Al_{OX}:Si_{OX} ratio remained constant (Table 3). The observed Al_{OX}:Si_{OX} molar ratios of 2.0-2.3 are consistent with SRO aluminosilicate, such as allophane and imogolite (Watanabe et al., 2023). Their formation during the current incubation is difficult to judge because we were not able to detect significant increase in extractable Si on bulk scale while significant increase in Si_{OX} phase from MF was found (Fig. 5c). The increased ratios over the incubation (Table 3), nonetheless, suggest a greater role of Fe_{Ox} phase such as ferrihydrite and nanocrystalline goethite relative to Si_{OX} for the assemblage formation in MF. Third, when comparing the two basalt treatments, significantly greater Fe_{OX} formation was shown in the fine basalt (Fig. 5b), indicating higher Fe dissolution (Table 3) due possibly to higher specific surface area (Table S2), more abundant OM (which likely includes organic acids), and/or slightly more alkaline pH (Table 4). The redox regime during the incubation may also be slightly different between the two basalt treatments as the basalt particle size should affect water and oxygen dynamics via texture/porosity difference, which might have affected Fe-OM interaction (Chen et al., 2020).

4.3 Influence of the size and chemical composition of crushed rock

Both the size and chemistry of crushed rock may control the formation of organo-mineral aggregates in MF. The mineral particle size likely played a significant role because the formation of MF including the accretion of OM and pedogenic metal phases occurred more in the fine basalt than the coarse basalt or other treatments (Fig. 3a, 3b; Fig. 5). In addition, the rock chemical composition likely contributed to the observed the retention of OM as organo-mineral assemblages in MF. Despite the same size class (38–75 μm) and similar particle size distribution (Fig. S1), the coarse basalt treatment led to significantly higher OM accretion in MF with a slightly lower C:N ratio compared to the granite treatment (Fig. 3b; Fig. 4a). In addition, the initial coarse basalt had more than one order of magnitude higher contents of PP- and especially OX-extractable metals (and Si_{OX}) than the initial granite (Table S2). Thus, the greater OM retention in the coarse basalt (Fig. 3b) may be attributable to the initial abundance of the reactive secondary minerals present. The increase in OM retention in the coarse basalt relative to the granite treatment (Fig. 3b), normalized to their difference in specific surface area (Table S2) translates to C loading of ca 0.1 mg C m^{-2}, which is well within the maximum sorptive capacity of the reactive secondary minerals (Wagai and Mayer, 2007; Schneider et al., 2010) and comparable to the C accretion on goethite in temperate field conditions

https://doi.org/10.5194/egusphere-2025-2840
Preprint. Discussion started: 10 July 2025

(Bramble et al., 2024). The significant contribution of secondary minerals present in the crushed basalt has also been shown in another incubation experiment conducted under slightly different conditions (Yang et al., under review). Our current study did not have a "fine-sized granite" treatment. Thus, a factorial design experiment is necessary to fully test the relative importance of mineral size and chemistry (weatherability) on the formation of organo-mineral assemblage.

4.4 Implications

Our experimental results from the artificial soil (the mineral-OM mixtures) may have implications for field soil processes. Weathering of fragmented rock in the presence of OM and microbial activity under a wet-and-dry cycle can occur during the early stages of pedogenesis (e.g., primary succession on glacial tills). Physical mixing and the severe wet-and-dry cycle used in this study may resemble conditions in agricultural topsoils. Recently, the application/mixing of crushed basalt and other mafic rocks to soils has drawn increasing attention as a method to remove atmospheric CO_2. The chemical weathering of basic rock releases divalent base cations (mainly Ca and Mg). These cations are partially balanced by carbonic acids that ultimately derive from atmospheric CO_2 (Beerling et al., 2020). Besides CO_2 removal, recent pot- and field-scale studies showed an apparent increase in soil OM upon the mixing of basic rock powders (Buss et al., 2024; Xu et al., 2024), although the lack of response was also reported (Yan et al., 2023; Sokol et al., 2024). Our results support the former studies. Mixing basaltic rock powder with organic amendments and soils likely increases the persistence of soil OM via organo-mineral assemblage formation. At the same time, however, the formation of basalt-OM aggregates likely slows down the rate of basalt weathering by physically protecting basalt surfaces (Yang et al., under review). Thus, further examination of the interactions among crushed rock, OM, and other soil particles is critical to predict the extent of CO_2 removal in enhanced rock weathering scenarios. Our study showed that the degree of OM accretion in MF (fine basalt > coarse basalt > granite > sand, Fig. 3b) corresponded to the content of Fe_{OX}, Al_{OX}, and Si_{OX} (Table S2; Fig. 5), which is likely attributed to the protective role of the reactive metal phases (esp. Fe_{OX}) and organo-metal coprecipitates formed more than the effect of pH (Table 4) or the bacterial copy number (Table S8). This finding may offer a mechanistic explanation for field-scale observations. First, previous studies (basaltic soils vs. granitic soils) have shown that the chemistry of parent rock strongly influences soil C storage at the landform scale (Orgill et al., 2017; Angst et al., 2018; Dutta et al., 2000; Mao et al., 2020). Basalt-derived soil had a significantly greater C accumulation at 0–30 cm depth (77 t ha^{-1}) compared with granite-derived soil (27–52 t ha^{-1}; Orgill et al., 2017). Another study further showed that the mean C accumulation in the upper 1-m depth soil was the highest in basalt landform (76.2 t C ha^{-1}), followed by alluvial (70.6 t C ha^{-1}), laterite (54.9 t C ha^{-1}), sandstone (48.0 t C ha^{-1}), and granite-gneiss (32.7 t C ha^{-1}) (Dutta et al., 2000). Second, the positive contribution of oxalate-extractable Fe and Al phases to soil C storage has been shown at a field scale (e.g., Fukumasu et al., 2021), regional to continental scales (Hughes, 1982; Ashida et al., 2021; von Fromm et al., 2021), up to a global scale (Rasmussen et al., 2018; von Fromm et al., 2025).

While the underlying mechanisms behind these associations require careful evaluation (Wagai and Mayer, 2007; Hall and Thompson, 2022; Fukumasu et al., 2025), the current results suggested a rapid formation of organo-mineral assemblage as meso-density aggregates. The mass of assemblages—estimated assuming ferrihydrite and allophane as the mineral components—accounted for roughly one-third of the total mass of the meso-density fraction (MF). It thus seems possible that the metal- and OM-rich assemblages formed are sticky enough to bind the other two-thirds of solids (organic and basalt particles) to form meso-density aggregates, in accord with the organo-metallic glue hypothesis (Wagai et al., 2020). While the relevance of current findings to field soil processes needs to be examined further, the current results help to elucidate the intimate interactions of microbes, their metabolites, and minerals in soil (Chorover, 2022; Fang et al., 2023; Wagai et al., 2023).

5 Conclusion

https://doi.org/10.5194/egusphere-2025-2840
Preprint. Discussion started: 10 July 2025

A formation of organo-mineral assemblages (as the meso-density fraction) from the mixture of crushed rocks and leaf compost was observed over the 55-day incubation with 8 wet-and-dry cycles. The fine basalt-OM mixture led to the highest formation of organo-mineral assemblages, followed by the coarse basalt and granite. The assemblage formation was promoted by (i) microbial re-working of OM (indicated by lower C:N and higher $\delta^{13}C$ and $\delta^{15}N$ compared to the original leaf compost) and (ii) the supply of extractable metals (esp. oxalate-extractable Fe phase) from the rock weathering. The chemistry of the meso-density materials formed was best characterized as coprecipitate enriched in both OM and oxalate-extractable Fe (and Al, Si). These findings supported the organo-metallic glue hypothesis (Wagai et al., 2020) and suggest that C accretion during early pedogenesis is likely to be driven in part by the formation of organo-mineral assemblages induced by the precipitation of short-range-order metal oxides through rock weathering.

Data availability. Not applicable.

Supplement. The supplement related to this article is available online at XXXX.

Author contributions. KM: investigation, methodology, writing (original draft preparation, review, and editing); JJ: investigation; HS: investigation; EM: investigation and writing (original draft preparation); RS: investigation and writing (review and editing); RW: conceptualization, writing (review and editing), funding acquisition, and supervision.

Competing interests. The authors declare that we have no known competing financial interests or personal relationships that could have appeared to influence the work reported in this paper.

Acknowledgements. The authors are grateful to Y. Yaegaki, R. Hirai, and Y. Yamashita for laboratory assistance, J. Fukumasu for the specific surface area analysis, K. Ito for the microbial community analysis, and Y. Nakayama for technical advice during the experiment. We also thank M. Bamba, S. Sato, and K. Minamisawa (Tohoku University) for 16S rRNA amplicon sequencing.

Financial support. This paper is based on results obtained from a project, JPNP18016, commissioned by the New Energy and Industrial Technology Development Organization (NEDO).

References

Angst, G., Messinger, J., Greiner, M., Häusler, W., Hertel, D., Kirfel, K., Kögel-Knabner, I., Leuschner, C., Rethemeyer, J., and Muellera, C.W.: Soil organic carbon stocks in topsoil and subsoil controlled by parent material, carbon input in the rhizosphere, and microbial-derived compounds, Soil Biol. Biochem., 122, 19–30, https://doi.org/10.1016/j.soilbio.2018.03.026, 2018.

Angst, G., Mueller, K. E., Castellano, M. J., Vogel, C., Wiesmeier, M., and Mueller, C. W.: Unlocking complex soil systems as carbon sinks: multi-pool management as the key. Nat. Commun., 14, 2967, https://doi.org/10.1038/s41467-023-38700-5, 2023.

Asano, M., and Wagai, R.: Evidence of aggregate hierarchy at micro- to submicron scales in an allophanic Andisol, Geoderma, 216, 62–74, https://doi.org/10.1016/j.geoderma.2013.10.005, 2014.

Ashida, K., Watanabe, T., Urayama, S., Hartono, A., Kilasara, M., Mvondo Ze, A. D., Nakao, A., Sugihara, S., and Funakawa, S.: Quantitative relationship between organic carbon and geochemical properties in tropical surface and subsurface soils, Biogeochemistry, 155, 77–95, https://doi.org/10.1007/s10533-021-00813-8, 2021.

https://doi.org/10.5194/egusphere-2025-2840
Preprint. Discussion started: 10 July 2025

Baldock, J. A., and Skjemstad, J. O.: Role of the soil matrix and minerals in protecting natural organic materials against biological attack, Org. Geochem, 31 (7–8), 697–710, https://doi.org/10.1016/S0146-6380(00)00049-8, 2000.

Bamba, M., Akyol, T. Y., Azuma, Y., Quilbe, J., Andersen, S. U., and Sato, S.: Synergistic effects of plant genotype and soil microbiome on growth in *Lotus japonicus*, FEMS Microbiol. Ecol., 100 (5), fiae056, https://doi.org/10.1093/femsec/fiae056, 2024.

Banfield, J. F., Barker, W. W., Welch, S. A., and Taunton, A.: Biological impact on mineral dissolution: Application of the lichen model to understanding mineral weathering in the rhizosphere, Proc. Natl. Acad. Sci. USA, 96 (7), 3404–3411, https://doi.org/10.1073/pnas.96.7.3404, 1999.

Basile-Doelsch, I., Balesdent, J., and Rose, J.: Are interactions between organic compounds and nanoscale weathering minerals the key drivers of carbon storage in soils?, Environ. Sci. Technol., 49 (7), 3997−3998, https://doi.org/10.1021/acs.est.5b00650, 2015.

Beerling, D. J., Kantzas, E. P., Lomas, M. R., Wade, P., Eufrasio, R. M., Renforth, P., Sarkar, B., Andrews, M. G., James, R. H., Pearce, C. R., Mercure, J. F., Pollitt, H., Holden, P. B., Edwards, N. R., Khanna, M., Koh, L., Quegan, S., Pidgeon, N. F., Janssens, I. A., Hansen, J., and Banwart, S. A.: Potential for large-scale CO_2 removal via enhanced rock weathering with croplands, Nature, 583, 242–248, https://doi.org/10.1038/s41586-020-2448-9, 2020.

Bhattacharjee, K., Barua, S., Chrungoo, N. K., and Joshi, S. R.: Characterization of biomineralizing and plant growth-promoting attributes of lithobiontic bacteria, Curr. Microbiol., 80, 80, https://doi.org/10.1007/s00284-022-03176-x, 2023.

Bramble, D. S. E., Ulrich, S., Schöning, I., Mikutta, R., Brandt, L., Poll, C., Kandeler, E., Mikutta, C., Konrad, A., Siemens, J., Yang, Y., Polle, A., Schall, P., Ammer, C., Kaiser, K., and Schrumpf, M.: Formation of mineral-associated organic matter in temperate soils is primarily controlled by mineral type and modified by land use and management intensity, Glob. Change Biol., 30, e17024, https://doi.org/10.1111/gcb.17024, 2024.

Bucka, F. B., Kölbl, A., Uteau, D., Peth, S., and Kögel-Knabner, I.: Organic matter input determines structure development and aggregate formation in artificial soils, Geoderma, 354, 113881, https://doi.org/10.1016/j.geoderma.2019.113881, 2019.

Bucka, F. B., Felde, V. J. M. N. L., Peth, S., and K¨ogel-Knabner, I.: Disentangling the effects of OM quality and soil texture on microbially mediated structure formation in artificial model soils, Geoderma, 403, 115213, https://doi.org/10.1016/j.geoderma.2021.115213, 2021.

Burghelea, C., Zaharescu, D. G., Dontsova, K., Maier, R., Huxman, T., and Chorover, J.: Mineral nutrient mobilization by plants from rock: Influence of rock type and arbuscular mycorrhiza, Biogeochemistry, 124, 187–203, https://doi.org/10.1007/s10533-015-0092-5, 2015.

Buss, W., Hasemer, H., Ferguson, S., and Borevitz, J.: Stabilisation of soil organic matter with rock dust partially counteracted by plants, Glob. Chang. Biol., 30 (1), e17052, https://doi.org/10.1111/gcb.17052, 2024.

Chapman, J. B., Weiss, D. J., Shan, Y., and Lemburger, M.: Iron isotope fractionation during leaching of granite and basalt by hydrochloric and oxalic acids, Geochim. Cosmochim. Acta, 73 (5), 1312–1324, https://doi.org/10.1016/j.gca.2008.11.037, 2009.

Chen, C., Dynes, J. J., Wang, J., Karunakaran, C., and Sparks, D. L.: Soft X-ray spectromicroscopy study of mineral-organic matter associations in pasture soil clay fractions, Environ. Sci. Technol., 48 (12), 6678–6686, https://doi.org/10.1021/es405485a, 2014.

Chen, C., Hall, S. J., Coward, E., and Thompson, A.: Iron-mediated organic matter decomposition in humid soils can counteract protection, Nat. Commun., 11, 2255, https://doi.org/10.1038/s41467-020-16071-5, 2020.

Choi, W. J., Kwak, J. H., Park, H. J., Yang, H. I., Park, S. I., Xu, Z., Lee, S. M., Lim, S. S., and Chang S. X.: Land-use type, and land management and disturbance affect soil $\delta^{15}N$: A review, J. Soils Sediments, 20, 3283–3299,

https://doi.org/10.5194/egusphere-2025-2840
Preprint. Discussion started: 10 July 2025

https://doi.org/10.1007/s11368-020-02708-x, 2020.

Chorover, J.: Microbe-biomolecule-mineral interfacial reactions, in: Multi-Scale Biogeochemical Processes in Soil Ecosystems: Critical Reactions and Resilience to Climate Changes, edited by: Yang, Y., Keiluweit, M., Senesi, N., and Xing, B., John Wiley & Sons, Inc., Hoboken, 117–140, https://doi.org/10.1002/9781119480419, 2022.

Cole, J. R., Wang, Q., Fish, J. A., Chai, B., McGarrell, D. M., Sun, Y., Brown, C. T., Porras-Alfaro, A., Kuske, C. R., and Tiedje, J. M.: Ribosomal Database Project: Data and tools for high throughput rRNA analysis, Nucleic Acids Res., 42 (D1), D633–D642, https://doi.org/10.1093/nar/gkt1244, 2014.

Cornell, R. M., and Schwertmann, U. (Eds.): The Iron Oxides: Structure, Properties, Reactions, Occurences and Uses, Wiley‐VCH Verlag GmbH & Co. KGaA, ISBN9783527602094, 2003.

Dutta, D., Sah, K. D., Reddy, R. S., Anil Kumar, K. S., and Koyal, A.: Soil organic carbon storage in different landforms of South Deccan plateau of Andhra Pradesh, J. Indian Soc. Soil Sci., 48 (3), 447–450, https://www.indianjournals.com/ijor.aspx?target=ijor:jisss&volume=48&issue=3&article=005, 2000.

Edgar, R. C.: SINTAX: A simple non-Bayesian taxonomy classifier for 16S and ITS sequences, bioRxiv, 074161, https://doi.org/10.1101/074161, 2016.

Fang, Q., Lu, A., Hong, H., Kuzyakov, Y., Algeo, T. J., Zhao, L., Olshansky, Y., Moravec, B., Barrientes, D. M., and Chorover, J.: Mineral weathering is linked to microbial priming in the critical zone, Nat. Commun., 14, 345, https://doi.org/10.1038/s41467-022-35671-x, 2023.

Farda, B., Djebaili, R., Del Gallo, M., Ercole, C., Bellatreccia, F., and Pellegrini, M.: The “Infernaccio” gorges: Microbial diversity of black deposits and isolation of manganese-solubilizing bacteria, Biol., 11 (8), 1204, https://doi.org/10.3390/biology11081204, 2022.

Finlay, R. D., Mahmood, S., Rosenstock, N., Bolou-Bi, E. B., Köhler, S. J., Fahad, Z. Rosling, A., Wallander, H., Belyazid, S., Bishop, K., and Lian, B.: Reviews and syntheses: Biological weathering and its consequences at different spatial levels – from nanoscale to global scale, Biogeosciences, 17 (6), 1507–1533, https://doi.org/10.5194/bg-17-1507-2020, 2020.

Friedlingstein, P., O'Sullivan, M., Jones, M. W., Andrew, R. M., Gregor, L., Hauck, J., Quéré, C. Le, Luijkx, I. T., Olsen, A., and Peters, G. P., et al.: Global Carbon Budget 2022, Earth Syst. Sci. Data, 14, 4811–4900, https://doi.org/10.5194/essd-14-4811-2022, 2022.

Fukumasu, J., Poeplau, C., Coucheney, E., Jarvis, N., Kl¨offel, T., Koestel, J., K¨atterer, T., Svensson, D. N., Wetterlind, J., and Larsbo, M.: Oxalate-extractable aluminum alongside carbon inputs may be a major determinant for organic carbon content in agricultural topsoils in humid continental climate, Geoderma, 402, 115345, https://doi.org/10.1016/j.geoderma.2021.115345, 2021.

Fukumasu, J., Yang, P. T., Kajiura, M., Gregorich, E., and Wagai, R.: Soil extraction with pyrophosphate-dithionite mixture: a practical method to estimate organic carbon associated with metal cations and reactive mineral phases, Soil Sci. Plant Nutr., 1–13, https://doi.org/10.1080/00380768.2024.2448861, 2025.

Golchin, A., Oades, J. M., Skjemstad, J. O., and Clarke, P.: Study of free and occluded particulate organic matter in soils by solid state ^{13}C Cp/MAS NMR spectroscopy and scanning electron microscopy, Aust. J. Soil Res., 32 (2), 285–309, https://doi.org/10.1071/SR9940285, 1994.

Goslee, S. C., and Urban, D. L.: The ecodist package for dissimilarity-based analysis of ecological data, J. Stat. Softw., 22 (7), 1–19, https://doi.org/10.18637/jss.v022.i07, 2007.

Gray, J., and Murphy, B.: Parent material and world soil distribution, in: Symposium no. 21, Proceedings of 17th World Congress of Soil Science, 2215, 1–14, 2002.

Hall, S. J., Ye, C., Weintraub, S. R., and Hockaday, W. C.: Molecular trade-offs in soil organic carbon composition at continental scale, Nat. Geosci., 13, 687–692, https://doi.org/10.1038/s41561-020-0634-x, 2020.

Hall, S. J., and Thompson, A.: What do relationships between extractable metals and soil organic carbon concentrations

https://doi.org/10.5194/egusphere-2025-2840
Preprint. Discussion started: 10 July 2025

mean?, Soil Sci. Soc. Am. J., 86, 195–208, https://doi.org/10.1002/saj2.20343, 2022.

Hara, S., Kakizaki, K., Bamba, M., Itakura, M., Sugawara, M., Suzuki, A., Sasaki, Y., Takeda, M., Tago, K., Ohbayashi, T., Aono, T., Aoyagi, L. N., Shimada, H., Shingubara, R., Masuda, S., Shibata, A., Shirasu, K., Wagai, R., Akiyama, H., Sato, S., and Minamisawa, K.: Does rhizobial inoculation change the microbial community in field soils? A comparison with agricultural land-use changes, Microbes Environ., 39 (3), ME24006, https://doi.org/10.1264/jsme2.ME24006, 2024.

Harter, R. D., and Naidu, R.: Role of metal-organic complexation in metal sorption by soils, Adv. Agron., 55, 219–263, https://doi.org/10.1016/S0065-2113(08)60541-6, 1995.

Hartmann, M., and Six, J.: Soil structure and microbiome functions in agroecosystems, Nat. Rev. Earth Environ., 4, 4–18, https://doi.org/10.1038/s43017-022-00366-w, 2023.

Hatton, P. J., Kleber, M., Zeller, B., Moni, C., Plante, A. F., Townsend, K., Gelhaye, L., Lajtha, K., and Derrien, D.: Transfer of litter-derived N to soil mineral-organic associations: Evidence from decadal ^{15}N tracer experiments, Org. Geochem., 42 (12), 1489–1501, https://doi.org/10.1016/j.orggeochem.2011.05.002, 2012.

Heckman, K., Lawrence, C. R., and Harden, J. W.: A sequential selective dissolution method to quantify storage and stability of organic carbon associated with Al and Fe hydroxide phases, Geoderma, 312, 24–35, https://doi.org/10.1016/j.geoderma.2017.09.043, 2018.

Heckman, K., Hicks Pries, C. E., Lawrence, C. R., Rasmussen, C., Crow, S. E., Hoyt, A. M., von Fromm, S. F., Shi, Z., Stoner, S., McGrath, C., Beem-Miller, J., Berhe, A. A., Blankinship, J. C., Keiluweit, M., Marín-Spiotta, E., Monroe, J. G., Plante, A. F., Schimel, J., Sierra, C. A., Thompson, A., and Wagai, R.: Beyond bulk: Density fractions explain heterogeneity in global soil carbon abundance and persistence, Glob. Chang Biol., 28 (3), 1178–1196, https://doi.org/10.1111/gcb.16023, 2022.

Hemingway, J. D., Rothman, D. H., Grant, K. E., Rosengard, S. Z., Eglinton, T. I., Derry, L. A., and Galy, V. V.: Mineral protection regulates long-term global preservation of natural organic carbon, Nature, 570, 228–231, https://doi.org/10.1038/s41586-019-1280-6, 2019.

Hiradate, S., Nakadai, T., Shindo, H., and Yoneyama, T.: Carbon source of humic substances in some Japanese volcanic ash soils determined by carbon stable isotopic ratio, $\delta^{13}C$, Geoderma, 119 (1–2), 133–141, https://doi.org/10.1016/S0016-7061(03)00257-X, 2004.

Hitchcock, A. P.: aXis 2000 - Analysis of X-ray Images and Spectra, http://unicorn.mcmaster.ca/aXis2000.html, 2023.

Horie, Y., Iwasaki, A., Tomoyose, N., Kido, M., Yamaguchi, T., Tada, K., Kawashita, H., Kohno, A., Hamamura, K., Yamazoe, R., Matsumoto, R., Yokoyama, S., Noguchi, I., Yagoh, H., Kai, I., Hamano, A., and Yoshida, F.: Acid deposition survey in Japan, phase 5 (2016). Journal of Environmental Laboratories Association, 41 (3), 2–37, http://db.cger.nies.go.jp/dataset/acidrain/ja/05/, 2016. (in Japanese).

Hughes, J. C.: High gradient magnetic separation of some soil clays from Nigeria, Brazil and Colombia. I. The interrelationships of iron and aluminium extracted by acid ammonium oxalate and carbon. Eur. J. Soil Sci., 33, 509–519, https://doi.org/10.1111/j.1365-2389.1982.tb01785.x, 1982.

IUSS Working Group WRB (Eds.): World Reference Base for Soil Resources 2014, update 2015: International soil classification system for naming soils and creating legends for soil maps, World Soil Resources Reports No. 106, FAO, Rome, 2015.

Jamoteau, F., Cam, N., Levard, C., Doelsch, E., Gassier, G., Duvivier, A., Boulineau, A., Saint-Antonin, F., and Basile-Doelsch, I.: Structure and chemical composition of soil C-rich Al−Si−Fe coprecipitates at nanometer scale, Environ. Sci. Technol., 57 (49), 20615−20626, https://doi.org/10.1021/acs.est.3c06557, 2023.

Kaiser, K., Guggenberger, G., Haumaier, L., and Zech, W.: Dissolved organic matter sorption on subsoils and minerals studied by ^{13}C-NMR and DRIFT spectroscopy. Eur. J. Soil Sci. 48 (2), 301–310, https://doi.org/10.1111/j.1365-2389.1997.tb00550.x, 1997.

https://doi.org/10.5194/egusphere-2025-2840
Preprint. Discussion started: 10 July 2025

Kleber, M., Eusterhues, K., Keiluweit, M., Mikutta, C., Mikutta, R., and Nico, P. S.: Chapter one - mineral–organic associations: Formation, properties, and relevance in soil environments, in: Advances in Agronomy, edited by: Sparks, D. L., Academic Press, Volume 130, 1–140, https://doi.org/10.1016/bs.agron.2014.10.005, 2015.

Koba, K., Kinoshita, K., Onishi, Y., Fukushima, K., Osaka, K., Matsuo, N., Funakawa, K., Seko, Y., Medo, A., Hirasawa, R., O Ogawa, N., Hyodo, F., and Yoshimizu, C.: Carbon and nitrogen isotope analysis on small samples using a near-conventional EA-IRMS system, Radioisotopes, 70 (4), 291–299, https://doi.org/10.3769/radioisotopes.70.291, 2021. (in Japanese).

Krause, L., Biesgen, D., Treder, A., Schweizer, S. A., Klumpp, E., Knief, C., and Siebers, N.: Initial microaggregate formation: Association of microorganisms to montmorillonite-goethite aggregates under wetting and drying cycles, Geoderma, 351, 250–260, https://doi.org/10.1016/j.geoderma.2019.05.001, 2019.

Lawrence, C. R., Harden, J. W., Xu, X., Schulz, M. S., and Trumbore, S. E.: Long-term controls on soil organic carbon with depth and time: A case study from the Cowlitz River Chronosequence, WA USA, Geoderma, 247–248, 73–87, https://doi.org/10.1016/j.geoderma.2015.02.005, 2015.

Lehmann, J., Bossio, D. A., Kögel-Knabner, I., and Rillig, M. C.: The concept and future prospects of soil health, Nat. Rev. Earth Environ., 1, 544–553, https://doi.org/10.1038/s43017-020-0080-8, 2020.

Liu, C., Cui, Y., Li, X., and Yao, M.: microeco: an R package for data mining in microbial community ecology, FEMS Microbiol. Ecol., 97 (2), fiaa255, https://doi.org/10.1093/femsec/fiaa255, 2021.

Lundström, U. S., van Breemen, N., and Bain, D.: The podzolization process. A review, Geoderma, 94 (2–4), 91–107, https://doi.org/10.1016/S0016-7061(99)00036-1, 2000.

Lybrand, R. A., Austin, J. C., Fedenko, J., Gallery, R. E., Rooney, E., Schroeder, P. A., Zaharescu, D. G., and Qafoku, O.: A coupled microscopy approach to assess the nano-landscape of weathering, Sci. Rep., 9, 5377, https://doi.org/10.1038/s41598-019-41357-0, 2019.

Mao, X., Van Zwieten, L., Zhang, M., Qiu, Z., Yao, Y., and Wang., H.: Soil parent material controls organic matter stocks and retention patterns in subtropical China, J. Soils Sediments, 20, 2426–2438, https://doi.org/10.1007/s11368-020-02578-3, 2020.

Martinelli, L. A., Piccolo, M. C., Townsend, A. R., Vitousek, P. M., Cuevas, E., McDowell, W., Robertson, G. P., Santos, O. C., and Treseder, K.: Nitrogen stable isotopic composition of leaves and soil: Tropical versus temperate forests, Biogeochemistry, 46, 45–65, https://doi.org/10.1007/BF01007573, 1999.

Masiello, C. A., Chadwick, O. A., Southon, J., Torn, M. S., and Harden, J. W.: Weathering controls on mechanisms of carbon storage in grassland soils, Global Biogeochem. Cycles, 18, GB4023, https://doi.org/10.1029/2004GB002219, 2004.

McMurdie, P. J., and Holmes, S.: phyloseq: An R package for reproducible interactive analysis and graphics of microbiome census data, PLoS ONE, 8 (4), e61217, https://doi.org/10.1371/journal.pone.0061217, 2013.

Moni, C., Derrien, D., Hatton, P. J., Zeller, B., and Kleber, M.: Density fractions versus size separates: Does physical fractionation isolate functional soil compartments?, Biogeosciences, 9 (12), 5181–5197, https://doi.org/10.5194/bg-9-5181-2012, 2012.

Ogawa, N. O., Nagata, T., Kitazato, H., and Ohkouchi, N.: Ultra-sensitive elemental analyzer/isotope ratio mass spectrometer for stable nitrogen and carbon isotope analyses, in: Earth, Life and Isotopes, edited by: Ohkouchi, N., Tayasu, I., and Koba, K., Kyoto University Press, pp. 339–353. ISBN: 9784876989607, 2010.

Oksanen, J.: Vegan: ecological diversity. R project, 368, 1–11, https://cran.r-project.org/web/packages/vegan/vignettes/diversity-vegan.pdf, 2013.

Orgill, S. E., Condon, J. R., Conyers, M. K., Morris, S. G., Murphy, B. W., and Greene, R. S. B.: Parent material and climate affect soil organic carbon fractions under pastures in south-eastern Australia, Soil Res., 55 (8), 799–808,

https://doi.org/10.5194/egusphere-2025-2840
Preprint. Discussion started: 10 July 2025

https://doi.org/10.1071/SR16305, 2017.

Parker, D. R.: Aluminum speciation, in: Encyclopedia of Soils in the Environment, edited by: Hillel, D., Elsevier, 50–56, https://doi.org/10.1016/B0-12-348530-4/00199-5, 2005.

Percival, H. J., Parfitt, R. L., and Scott, N. A.: Factors controlling soil carbon levels in New Zealand grasslands is clay content important?, Soil Sci. Soc. Am. J., 64 (5), 1623–1630, https://doi.org/10.2136/sssaj2000.6451623x, 2000.

Philippot, L., Chenu, C., Kappler, A., Rillig, M. C., and Fierer, N.: The interplay between microbial communities and soil properties, Nat. Rev. Microbiol., 22, 226–239, https://doi.org/10.1038/s41579-023-00980-5, 2024.

Prietzel, J., Müller, S., Kögel-Knabner, I., Thieme, J., Jaye, C., and Fischer, D.: Comparison of soil organic carbon speciation using C NEXAFS and CPMAS ^{13}C NMR spectroscopy, Sci. Total Environ., 628–629, 906–918, https://doi.org/10.1016/j.scitotenv.2018.02.121, 2018.

Pronk, G. J., Heister, K., Vogel, C., Babin, D., Bachmann, J., Ding, G. C., Ditterich, F., Gerzabek, M. H., Giebler, J., Hemkemeyer, M., Kandeler, E., Mouvenchery, Y. K., Miltner, A., Poll, C., Schaumann, G. E., Smalla, K., Steinbach, A., Tanuwidjaja, I., Tebbe, C. C., Wick, L. Y., Woche, S. K., Totsche, K. U., Schloter, M., and Kögel-Knabner, I.: Interaction of minerals, organic matter, and microorganisms during biogeochemical interface formation as shown by a series of artificial soil experiments, Biol. Fertil. Soils, 53, 9–22, https://doi.org/10.1007/s00374-016-1161-1, 2017.

Rabot, E., Wiesmeier, M., Schlüter, S., and Vogel, H. -J.: Soil structure as an indicator of soil functions: A review, Geoderma, 314, 122–137, https://doi.org/10.1016/j.geoderma.2017.11.009, 2018.

Rasmussen, C., Heckman, K., Wieder, W. R., Keiluweit, M., Lawrence, C. R., Berhe, A. A., Blankinship, J. C., Crow, S. E., Druhan, J. L., and Pries, C. E. H. et al.: Beyond clay: towards an improved set of variables for predicting soil organic matter content, Biogeochemistry, 137, 297–306, https://doi.org/10.1007/s10533-018-0424-3, 2018.

Rasmussen, C., Torn, M. S., and Southard, R. J.: Mineral assemblage and aggregates control carbon dynamics in a California conifer forest, Soil Sci. Soc. Am. J., 69 (6), 1711–1721, https://doi.org/10.2136/sssaj2005.0040, 2005.

Regelink, I. C., Stoof, C. R., Rousseva, S., Weng, L., Lair, G. J., Kram, P., Nikolaidis, N. P., Kercheva, M., Banwart, S., and Comans, R. N. J.: Linkages between aggregate formation, porosity and soil chemical properties, Geoderma, 247–248, 24–37, https://doi.org/10.1016/j.geoderma.2015.01.022, 2015.

Rennert, T.: Wet-chemical extractions to characterise pedogenic Al and Fe species – a critical review, Soil Res., 57, 1–16, https://doi.org/10.1071/SR18299, 2019.

Saidy, A. R., Smernik, R. J., Baldock, J. A., Kaiser, K., and Sanderman, J.: Microbial degradation of organic carbon sorbed to phyllosilicate clays with and without hydrous iron oxide coating, Eur. J. Soil Sci., 66 (1), 83–94, https://doi.org/10.1111/ejss.12180, 2015.

Schlüter, S., Sammartino, S., and Koestel, J.: Exploring the relationship between soil structure and soil functions via pore-scale imaging, Geoderma, 370, 114370, https://doi.org/10.1016/j.geoderma.2020.114370, 2020.

Schneider, M. P. W., Scheel, T., Mikutta, R., van Hees, P., Kaiser, K., and Kalbitz, K.: Sorptive stabilization of organic matter by amorphous Al hydroxide, Geochim Cosmochim Acta., 74, 1606–1619, https://doi.org/10.1016/j.gca.2009.12.017, 2010.

Shang, C., and Tiessen, H.: Organic matter stabilization in two semiarid tropical soils: Size, density, and magnetic separations, Soil Sci. Soc. Am. J., 62 (5), 1247–1257, https://doi.org/10.2136/sssaj1998.03615995006200050015x, 1998.

Shimada, H., Wagai, R., Inoue, Y., Tamura, K., and Asano, M.: Millennium timescale carbon stability in an Andisol: How persistent are organo-metal complexes?, Geoderma, 417, 115820, https://doi.org/10.1016/j.geoderma.2022.115820, 2022.

Soil Survey Staff. (Eds.): Keys to Soil Taxonomy, 12th ed, USDA-Natural Resources Conservation Service, Washington, DC, 2014.

Sokol, N. W., Sohng, J., Moreland, K., Slessarev, E., Goertzen, H., Schmidt, R., Samaddar, S., Holzer, I., Almaraz, M., Geoghegan, E., Houlton, B., Montañez, I., Pett-Ridge, J., and Scow, K.: Reduced accrual of mineral-associated organic

https://doi.org/10.5194/egusphere-2025-2840
Preprint. Discussion started: 10 July 2025

matter after two years of enhanced rock weathering in cropland soils, though no net losses of soil organic carbon, Biogeochemistry, 167, 989–1005, https://doi.org/10.1007/s10533-024-01160-0, 2024.

Sollins, P., Homann, P., and Caldwell, B. A.: Stabilization and destabilization of soil organic matter: mechanisms and controls, Geoderma, 74 (1–2), 65–105, https://doi.org/10.1016/S0016-7061(96)00036-5, 1996.

Sollins, P., Kramer, M. G., Swanston, C., Lajtha, K., Filley, T., Aufdenkampe, A. K., Wagai, R., and Bowden, R. D.: Sequential density fractionation across soils of contrasting mineralogy: Evidence for both microbial- and mineral-controlled soil organic matter stabilization, Biogeochemistry, 96, 209–231, https://doi.org/10.1007/s10533-009-9359-z, 2009.

Solomon, D., Lehmann, J., Harden, J., Wang, J., Kinyangi, J., Heymann, K., Karunakaran, C., Lu, Y., Wirick, S., and Jacobsen, C.: Micro- and nano-environments of carbon sequestration: Multi-element STXM–NEXAFS spectromicroscopy assessment of microbial carbon and mineral associations, Chem. Geol., 329, 53–73, https://doi.org/10.1016/j.chemgeo.2012.02.002, 2012.

Sørensen, L. H.: Stabilization of newly formed amino acid metabolites in soil by clay minerals, Soil Sci., 114 (1), 5–11, https://doi.org/10.1097/00010694-197207000-00002, 1972.

Suzuki, M. T., Taylor, L. T., and DeLong, E. F.: Quantitative analysis of small-subunit rRNA genes in mixed microbial populations via 5′-nuclease assays. Appl. Environ. Microbiol., 66 (11), 4605–4614, https://doi.org/10.1128/AEM.66.11.4605-4614.2000, 2000.

Takahashi, T., and Dahlgren, R. A.: Nature, properties and function of aluminum–humus complexes in volcanic soils, Geoderma, 263, 110–121, https://doi.org/10.1016/j.geoderma.2015.08.032, 2016.

Takeichi, Y., Inami, N., Suga, H., Miyamoto, C., Ueno, T., Mase, K., Takahashi, Y., and Ono, K.: Design and performance of a compact scanning transmission X-ray microscope at the Photon Factory, Rev. Sci. Instrum., 87 (1), 013704, https://doi.org/10.1063/1.4940409, 2016.

Tamrat, W. Z., Rose, J., Grauby, O., Doelsch, E., Levard, C., Chaurand, P., and Basile-Doelsch, I.: Composition and molecular scale structure of nanophases formed by precipitation of biotite weathering products, Geochim. Cosmochim. Acta, 229, 53–64, https://doi.org/10.1016/j.gca.2018.03.012, 2018.

Tamrat, W. Z., Rose, J., Grauby, O., Doelsch, E., Levard, C., Chaurand, P., and Basile-Doelsch, I.: Soil organo-mineral associations formed by co-precipitation of Fe, Si and Al in presence of organicligands, Geochim. Cosmochim. Acta, 260, 15–28, https://doi.org/10.1016/j.gca.2019.05.043, 2019.

Tipping, E.: The adsorption of aquatic humic substances by iron oxides, Geochim. Cosmochim. Acta, 45 (2), 191–199, https://doi.org/10.1016/0016-7037(81)90162-9, 1981.

Torn, M. S., Trumbore, S. E., Chadwick, O. A., Vitousek, P. M., and Hendricks, D. M.: Mineral control of soil organic carbon storage and turnover, Nature, 389, 170–173, https://doi.org/10.1038/38260, 1997.

Totsche, K. U., Amelung, W., Gerzabek, M. H., Guggenberger, G., Klumpp, E., Knief, C., Lehndorff, E., Mikutta, R., Peth, S., Prechtel, A., Ray, N., and Kögel-Knabner, I.: Microaggregates in soils, J. Plant Nutr. Soil Sci., 181, 104–136, https://doi.org/10.1002/jpln.201600451, 2018.

Uroz, S., Kelly, L. C., Turpault, M. P., Lepleux, C., and Frey-Klett, P.: The mineralosphere concept: Mineralogical control of the distribution and function of mineral-associated bacterial communities, Trends Microbiol., 23 (12), 751–762, https://doi.org/10.1016/j.tim.2015.10.004, 2015.

Vogel, C., Babin, D., Pronk, G. J., Heister, K., Smalla, K., and Kögel-Knabner, I.: Establishment of macro-aggregates and organic matter turnover by microbial communities in long-term incubated artificial soils, Soil Biol. Biochem., 79, 57–67, https://doi.org/10.1016/j.soilbio.2014.07.012, 2014.

von Fromm, S. F., Hoyt, A. M., Lange, M., Acquah, G. E., Aynekulu, E., Berhe, A. A., Haefele, S. M., McGrath, S. P., Shepherd, K. D., Sila, A. M., Six, J., Towett, E. K., Trumbore, S. E., Vågen, T.-G., Weullow, E., Winowiecki, L. A., and

https://doi.org/10.5194/egusphere-2025-2840
Preprint. Discussion started: 10 July 2025

Doetterl, S.: Continental-scale controls on soil organic carbon across sub-Saharan Africa, SOIL, 7, 305–332, https://doi.org/10.5194/soil-7-305-2021, 2021.

von Fromm, S. F., Jungkunst, H. F., Amenkhienan, B., Hall, S. J., Georgiou, K., Pries, C. H., Montaño-López, F., Quesada, C. A., Rasmussen, C., Schrumpf, M., Singh, B., Thompson, A., Wagai, R., and Fiedler, S.: Moisture and soil depth govern relationships between soil organic carbon and oxalate-extractable metals at the global scale, Biogeochemistry, 168, 20, https://doi.org/10.1007/s10533-025-01208-9, 2025.

Wagai, R., and Sollins, P.: Biodegradation and regeneration of water-soluble carbon in a forest soil: Leaching column study, Biol. Fertil. Soils, 35, 18–26, https://doi.org/10.1007/s00374-001-0434-4, 2002.

Wagai, R., and Mayer, L.M.: Sorptive stabilization of organic matter in soils by hydrous iron oxides, Geochim. Cosmochim. Acta, 71 (1), 25–35, https://doi.org/10.1016/j.gca.2006.08.047, 2007.

Wagai, R., Kishimoto-Mo, A. W., Yonemura, S., Shirato, Y., Hiradate, S., and Yagasaki, Y.: Linking temperature sensitivity of soil organic matter decomposition to its molecular structure, accessibility, and microbial physiology, Glob. Chang. Biol., 19 (4), 1114–1125, https://doi.org/10.1111/gcb.12112, 2013a.

Wagai, R., Mayer, L. M., Kitayama, K., and Shirato, Y.: Association of organic matter with iron and aluminum across a range of soils determined via selective dissolution techniques coupled with dissolved nitrogen analysis, Biogeochemistry, 112, 95–109, https://doi.org/10.1007/s10533-011-9652-5, 2013b.

Wagai, R., Kajiura, M., Asano, M., and Hiradate, S.: Nature of soil organo-mineral assemblage examined by sequential density fractionation with and without sonication: Is allophanic soil different?, Geoderma, 241–242, 295–305, https://doi.org/10.1016/j.geoderma.2014.11.028, 2015.

Wagai, R., Kajiura, M., Uchida, M., and Asano, M.: Distinctive roles of two aggregate binding agents in allophanic Andisols: Young carbon and poorly-crystalline metal phases with old carbon, Soil Syst., 2 (2), 29, https://doi.org/10.3390/soilsystems2020029, 2018.

Wagai, R., Kajiura, M., and Asano, M.: Iron and aluminum association with microbially processed organic matter via meso-density aggregate formation across soils: Organo-metallic glue hypothesis, SOIL, 6 (2), 597–627, https://doi.org/10.5194/soil-6-597-2020, 2020.

Wagai, R., Yang, P. T., and Kaiser, K.: Interfacial reactions of microorganisms with minerals and organic matter, in: Encyclopedia of Soils in the Environment (Second Edition), edited by: Goss, M. J., and Oliver, M., Academic Press, 458–469, https://doi.org/10.1016/B978-0-12-822974-3.00232-9, 2023.

Watanabe, T., Harsh, J. B., and Wagai, R.: Short-range ordered aluminosilicates, in: Encyclopedia of Soils in the Environment (Second Edition), edited by: Goss, M. J., and Oliver, M., Academic Press, 121–134, https://doi.org/10.1016/B978-0-12-822974-3.00223-8, 2023.

Wattel-Koekkoek, E. J. W., Buurman, P., Van der Plicht, J., Wattel, E., and Van Breemen, N.: Mean residence time of soil organic matter associated with kaolinite and smectite, Eur. J. Soil Sci., 54 (2), 269–278, https://doi.org/10.1046/j.1365-2389.2003.00512.x, 2003.

Xu, T., Yuan, Z., Vicca, S., Goll, D. S., Li, G., Lin, L., Chen, H., Bi, B., Chen, Q., Li, C., Wang, X., Wang, C., Hao, Z., Fang, Y., and Beerling, D. J.: Enhanced silicate weathering accelerates forest carbon sequestration by stimulating the soil mineral carbon pump, Glob. Change Biol., 30 (8), e17464, https://doi.org/10.1111/gcb.17464, 2024.

Yan, Y., Dong, X., Li, R., Zhang, Y., Yan, S., Guan, X., Yang, Q., Chen, L., Fang, Y., Zhang, W., and Wang, S.: Wollastonite addition stimulates soil organic carbon mineralization: Evidences from 12 land-use types in subtropical China, Catena, 225, 107031, https://doi.org/10.1016/j.catena.2023.107031, 2023.

Yudina, A., and Kuzyakov, Y.: Dual nature of soil structure: The unity of aggregates and pores, Geoderma, 434, 116478, https://doi.org/10.1016/j.geoderma.2023.116478, 2023.